

A heterogeneous III-V/silicon integration platform for on-chip quantum photonic circuits with single quantum dot devices

Marcelo Davanco,^{1,*} Jin Liu,^{1,2,3,†} Luca Sapienza,^{1,4} Chen-Zhao Zhang,⁵ José Vinícius De Miranda Cardoso,^{1,6} Varun Verma,⁷ Richard Mirin,⁷ Sae Woo Nam,⁷ Liu Liu,⁵ and Kartik Srinivasan^{1,‡}

¹Center for Nanoscale Science and Technology, National Institute of Standards and Technology, Gaithersburg, MD 20899, USA

²Maryland NanoCenter, University of Maryland, College Park, USA

³School of Physics, Sun-Yat Sen University, Guangzhou, 510275, China

⁴Department of Physics & Astronomy, University of Southampton S017 1BJ, UK

⁵South China Academy of Advanced Optoelectronics, Science Building No. 5, South China Normal University, Higher-Education Mega-Center, Guangzhou 510006, China

⁶Federal University of Campina Grande, Brazil

⁷National Institute of Standards and Technology, Boulder, CO 80305, USA

(Dated: November 16, 2021)

Photonic integration is an enabling technology for photonic quantum science, offering greater scalability, stability, and functionality than traditional bulk optics. Here, we describe a scalable, heterogeneous III-V/silicon integration platform to produce Si_3N_4 photonic circuits incorporating GaAs-based nanophotonic devices containing self-assembled InAs/GaAs quantum dots. We demonstrate pure single-photon emission from individual quantum dots in GaAs waveguides and cavities - where strong control of spontaneous emission rate is observed - directly launched into Si_3N_4 waveguides with $> 90\%$ efficiency through evanescent coupling. To date, InAs/GaAs quantum dots constitute the most promising solid-state triggered single-photon sources, offering bright, pure and indistinguishable emission that can be electrically and optically controlled. Si_3N_4 waveguides offer low-loss propagation, tailorable dispersion and high Kerr nonlinearities, desirable for linear and nonlinear optical signal processing down to the quantum level. We combine these two in an integration platform that will enable a new class of scalable, efficient and versatile integrated quantum photonic devices.

Although the increasing complexity of quantum photonic circuits has enabled small-scale demonstrations of quantum computation, simulations, and metrology^{1,2}, the development of highly-integrated systems that can solve more complex problems³ is severely limited by system inefficiencies. In circuits that are, by and large, composed of purely passive elements such as waveguide arrays, phase delays, and beamsplitters, a combination of small photon flux at the circuit input, passive losses in the circuit, and inefficient detection at the output leads to unrealistically long times for large-scale experiments⁴. While losses within the photonic circuit can be minimized through an appropriate choice of materials and waveguide architectures, and single-photon detection with almost 100% efficiency is now possible with superconducting single-photon detectors²¹, the availability of a large on-chip single-photon flux is still a significant bottleneck. Overcoming such a limitation can enable not only further scaling of photonic quantum information experiments, but also quantum-level investigation of a variety of physical processes in nanophotonic and nanoplasmonic structures, such as Kerr nonlinearities⁷, optomechanical interactions⁷ and single-photon nonlinearities⁸⁻¹².

The on-chip photon flux problem can be broken down into two components - low single-photon generation rates and low coupling efficiency from external sources into the chip. Single quantum dots (QDs) in microcavities have recently been shown to be capable of providing on-demand, pure, highly indistinguishable single-photons at high rates^{13,14}, exceeding the performance of non-deterministic sources based on spontaneous nonlinear optical processes, and thus constitute a promising alternative to the source brightness issue. Neverthe-

less, coupling losses from free-space or optical fibers into the photonic circuit are still considerable. Although much effort is being devoted to improving the external source coupling efficiency, both in classical^{15,16} and quantum^{17,18} photonic experiments, it can be argued that such approaches, aimed at probing individual devices on a chip, do not allow for highly complex circuits. A scalable alternative is to instead create on-chip sources that are directly integrated into the passive waveguide network. This approach is in fact being pursued with spontaneous four-wave-mixing-type sources in silicon-based photonic circuits¹⁹, and in GaAs waveguide devices with QD on-chip sources¹⁻⁴. In the former approach, which benefits from low-loss propagation in the silicon waveguides, the fundamental tradeoff between source brightness and purity limits the generated photon flux, and may require complex multiplexing schemes to produce quasi-deterministic sources^{24,25}. In the latter case, which benefits from the availability of deterministic, high single-photon generation rates, propagation losses in the etched GaAs waveguides, considerably higher than in their silicon-based counterparts, limit on-chip photon routing, delay and interference; furthermore, the exclusive use of III-V materials in these architectures imposes challenging limits on device compactness, operation and performance (see SI for an extended discussion). Here, we present a photonic integration architecture that incorporates the benefits of these two approaches, and circumvents the aforementioned disadvantages. We have developed a scalable, integrated, heterogeneous III-V / silicon photonic platform to produce photonic circuits based on Si_3N_4 waveguides that directly incorporate GaAs nanophotonic devices, such as waveguides, ring resonators, and photonic crystals, containing single self-

assembled InAs/GaAs QDs. As illustrated in Figs. 1a and 1b, our integration platform allows the creation of passive, Si₃N₄ waveguide-based circuits, which can be used for low-loss routing, distribution and interference of light across the chip. At select portions of such passive circuits, GaAs waveguide-based nanophotonic devices containing self-assembled InAs QDs are produced, on top of a Si₃N₄ waveguide section. Such active GaAs devices can be designed to efficiently launch individual photons produced by the embedded QDs directly into the underlying Si₃N₄ guide, acting as efficient on-chip triggered single-photon sources for the Si₃N₄ waveguide circuit.

Self-assembled InAs/GaAs QDs have been used to demonstrate close-to-optimal triggered single-photon emission^{13,14}, spin-qubit operation²⁶, and a variety of strong-coupling cavity quantum electrodynamics (QED) systems^{8,12,27}. The two-level system nature of these QDs, together with the ability to integrate them within nanophotonic devices, may ultimately form the basis of deterministic quantum gates. As a complementary technology, Si₃N₄ waveguides offer low-loss propagation with tailorable dispersion and relatively high Kerr nonlinearities. These properties are currently being explored for linear²⁸ and nonlinear⁷ optical signal processing, as well as cavity optomechanics-based measurements²⁹, down to the quantum level.

Our work extends the application space of a mature, scalable, top-down heterogeneous photonic integrated circuit platform³⁰ into the quantum realm. Other heterogeneous integration platforms for quantum photonics have been developed, in which silicon served only as a substrate and had no photonic function, through epitaxial growth of InAs/GaAs QDs on silicon³¹, or flip-chip bonding of QD-containing GaAs nanomembranes³². Bottom-up or hybrid techniques¹⁵⁻¹⁷, where nanostructures containing quantum emitters are produced separately and then transferred onto a photonic circuit have also been developed. In contrast to all of these, our approach allows nearly independent, flexible, and high-resolution tailoring of both active (III-V) and passive (silicon) photonic waveguide elements with precise and repeatable, sub-100 nm alignment defined lithographically. All of these characteristics meet the critical requirements for scalable integrated quantum photonic systems. Our platform is also amenable to electrical injection operation as shown in ref. 36, along with all the aforementioned advantages offered by high performance single self-assembled QDs.

Quantum dot interface design The schematic drawings in Fig. 1c and Fig. 1d respectively show cross-sections of passive and active waveguide sections that form the building blocks of our photonic integration platform. Passive sections consist of Si₃N₄ ridges with SiO₂ and air for bottom and top claddings respectively. Active sections consist of the same Si₃N₄ ridge, topped by a GaAs ridge containing a single InAs QD. Single-photon sources are created from active sections as indicated in Fig. 1b. The GaAs and Si₃N₄ ridge widths are varied along z over two separate sections, with complementary functions. The emission capture section collects light radiated by the QD into a guided wave confined to the GaAs ridge, and the mode transformer transfers light from the GaAs into the Si₃N₄ ridge.

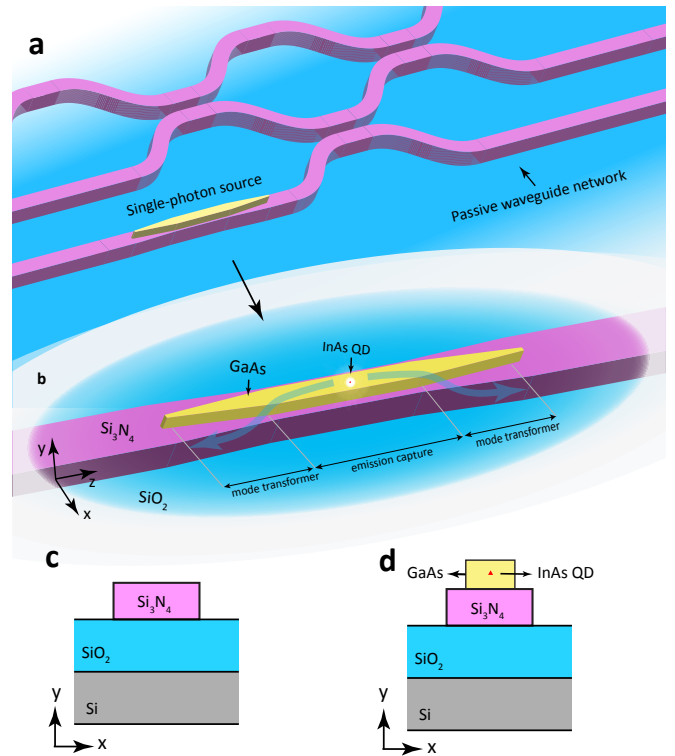


FIG. 1: Principle of operation and device geometry. **a**, Conceptual quantum photonic circuit composed of a passive waveguide network with a small, directly integrated nanophotonic single-photon source. **b**, Schematic showing geometry and operation principle of the integrated single-photon source shown in **a**. The source is composed of a single InAs QD embedded in a GaAs waveguide-based nanophotonic structure designed to efficiently capture QD emission and launch it directly into the Si₃N₄ waveguide. **c** and **d**: Cross-sections of passive Si₃N₄ and active GaAs waveguides that form the core elements of the integration platform.

We note that the source here is symmetric, so emission is in either $\pm z$ direction; unidirectional emission can be implemented with an end mirror or through chiral coupling³⁷. Design guidelines for the two sections are given in the following.

In the emission capture section, the widths of both waveguides are kept constant. The GaAs waveguide must support a single transverse-electric (TE) mode, and must be non-phase-matched to the Si₃N₄ guide. This ensures that the fundamental TE supermode of the waveguide stack is strongly concentrated in the GaAs core, as shown in the left panel in Fig. 2a. The InAs QD must then be made to radiate almost exclusively into the fundamental GaAs supermode, rather than into other guided or unbound modes of the stack. The ratio of the total dipole-emitted power that is coupled to the GaAs mode is the β -factor, $0 \leq \beta \leq 1$. $\beta \rightarrow 1$ can be achieved for guided modes in waveguides with high refractive index contrasts and sub-wavelength cross-sections, a result of strong field screening inside the guiding core, that takes place for radiative modes³⁸. This has been demonstrated in GaAs nanowires or nanowaveguides surrounded by air^{6,17,39} or encapsulated in SiN¹⁵. We predict similar performance for a

GaAs nanowire on top of a Si_3N_4 ridge. Assuming a horizontally (x) oriented QD electric dipole moment, we use finite difference time domain (FDTD) simulations to compute β for the GaAs supermode of an active guide designed for emission wavelengths near 1100 nm. The thicknesses of the GaAs and Si_3N_4 layers were taken from the wafer stack used for fabrication (see Methods and SI). Figure 2b shows a contour map of β as a function of wavelength and GaAs waveguide width, for a Si_3N_4 waveguide thickness of 580 nm and width of 600 nm. For GaAs widths between 300 nm and 400 nm, $0.37 > \beta > 0.35$ for waves traveling in either the $+z$ or $-z$ direction ($0.74 > 2 \cdot \beta > 0.70$ total) is achievable over ≈ 100 nm around 1100 nm. Further simulations (not shown) indicate that β is robust with respect to the Si_3N_4 waveguide width, to within several tens of nm. Although β is less than the maximum of 0.5 for symmetric emission, we note that both in simulations and in our devices the QD was located at a non-optimal vertical location inside the GaAs. In the SI, we provide similar simulations for an optimized geometry with $\beta > 0.45$ ($2\beta > 0.9$), comparable to those predicted in GaAs nanowires and nanowaveguides^{6,17,39}, and in photonic crystal (PhC) slow-light waveguides^{41,42}. We note nevertheless that the capture section can be replaced by any type of waveguide-based device, such as PhC or microring resonators (demonstrated below), which may provide high β through Purcell enhancement.

The mode transformer section consists of an adiabatic structure in which the widths of the GaAs and Si_3N_4 waveguides are, respectively, reduced and increased along the z -direction. The width tapers are designed such that the two waveguides become phase-matched over some finite length along the mode converter, where power is efficiently transferred from the GaAs to the Si_3N_4 guide; past the phase-matching length, the taper brings the two guides again away from the phase-matching condition, preventing the power from returning to the top guide. This is illustrated in the middle panel of Fig. 2a, which shows the FDTD simulated electric field distribution for a transformer in which the GaAs and Si_3N_4 widths vary linearly from 300 nm to 100 nm and from 800 nm to 600 nm respectively, over a length of $20 \mu\text{m}$. Significantly shorter lengths can potentially be achieved with more sophisticated profiles⁴³. Figure 2c shows modal power conversion efficiency from the GaAs mode to the Si_3N_4 mode (right panel of Fig. 2a) as function of wavelength (see Methods for simulation details). Maximum efficiency in excess of 98 % is achieved over a > 200 nm wavelength range. The geometry is robust to variations of tens of nm in the initial and final widths, well within electron-beam lithography tolerances.

With these two elements, the maximum efficiency of our ideal single-photon source is $\beta \cdot \eta \approx 0.72$ into both directions of the Si_3N_4 waveguide, or 36 % in either the $+z$ or $-z$ direction. For the optimized design in the SI, efficiency > 90 % could potentially be achieved. We now describe the fabrication of the devices just discussed.

Heterogenous device integration We start with the wafer stack shown in Fig. 3a. It consists of a silicon substrate topped by a $3 \mu\text{m}$ thick thermal oxide layer, a 550 nm layer

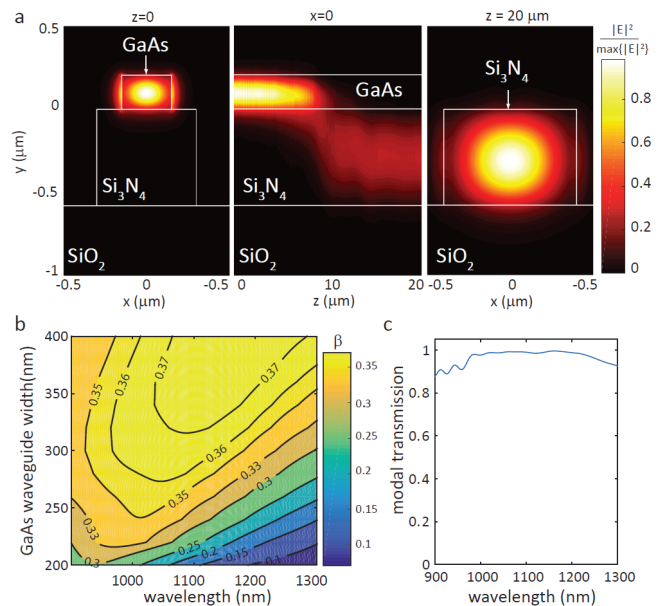


FIG. 2: **Nanophotonic design.** **a**, Left panel: Electric field distribution for the fundamental TE GaAs supermode of the waveguide stack in Fig. 1d, with dimensions specified in the main text. Center panel: Electric field distribution across the mode-transformer cross-section, for a GaAs mode launched at $z = 0$. At $z \approx 10 \mu\text{m}$, the GaAs and Si_3N_4 guides are phase-matched, and power is efficiently transferred from the top GaAs to the bottom Si_3N_4 guide. Right panel: Fundamental TE mode of the Si_3N_4 waveguide at the end of the mode transformer. **b**, Coupling efficiency (β), as a function of GaAs width and emission wavelength, of photons emitted by a dipole located at $x=0$ and 74 nm below the top surface, into the GaAs waveguide mode traveling in either the $+z$ or $-z$ direction. **c**, Modal power conversion efficiency from the GaAs mode into the Si_3N_4 mode in **a**, as a function of wavelength.

of stoichiometric Si_3N_4 , and an epitaxially grown 200 nm GaAs/AlGaAs stack containing a single layer of InAs quantum dots-in-a-well (DWELL)⁴⁴ located 74 nm below the top GaAs surface (details in the SI). As a result of the self-assembled growth, quantum dots were randomly distributed within this layer, with a density $> 100 / \mu\text{m}^2$. The hybrid III-V semiconductor / Si_3N_4 stack is produced with a low-temperature, oxygen plasma-activated wafer bonding procedure³⁰ detailed in the SI. Following the wafer bonding step, fabrication proceeds as in Figs. 3b and 3c (optical micrographs of the devices after completion of each step are also shown). An array of Au alignment marks is first produced on top of the GaAs layer via electron-beam lithography followed by metal lift-off. Electron-beam lithography and inductively-coupled plasma etching are next used to define GaAs devices aligned to the Au mark array. After cleanup of the etched sample surface, electron-beam lithography referenced to the same Au mark array is performed to define Si_3N_4 waveguide patterns aligned to the previously etched GaAs devices. Reactive ion etching is then used to produce the Si_3N_4 waveguides. As a final step, the chip is cleaved perpendicularly to the Si_3N_4 waveguides > 1 mm away from the GaAs devices, to allow

access with optical fibers in the endfire configuration. Before cleaving, 168 devices were produced, with a $> 80\%$ overall yield considering just device geometry. Features as small as 50 nm were achieved in the GaAs layer, and alignment accuracy on the order of a few tens of nm between the top and bottom waveguides was typically observed. We point out that, although here we had no control over QD location within the fabricated GaAs devices, we have specifically tailored our fabrication sequence to allow seamless incorporation of positioning techniques capable of spatially mapping QDs with respect to the Au marks^{13,46}.

Figure 3d is a false-color scanning electron micrograph (SEM) of a fabricated stacked-waveguide structure, corresponding to the tip of a mode transformer section. GaAs, Si_3N_4 and SiO_2 are colored in yellow, pink and blue respectively. Figures 3e and 3f show SEMs of two types of fabricated devices, with different emission capture geometries. In Fig. 3e, the capture structure is a straight waveguide as discussed above. The insets show details of the capture and mode transformer sections. In Fig. 3f, the capture structure is a GaAs microring resonator that is evanescently coupled to a bus waveguide with mode transformers, with the same geometry as in Fig. 3e. Here, QD emission coupled to whispering-gallery modes of the GaAs microring are outcoupled through the bus waveguide (coupling region shown in the inset), and then transferred to the Si_3N_4 guide via the mode transformers. We next describe optical measurements done to characterize the photonic performance of the fabricated devices.

Mode transformer characterization Two important parameters common to all types of devices are the mode transformer efficiency η and the external coupling efficiency η_{ext} . The first determines, together with the β -factor, the efficiency of the interface between the QD-containing GaAs layer and the passive waveguide circuit. The latter is the efficiency with which the device can be accessed from off-chip, ultimately determining the absolute power available for detection.

We estimate the mode transformer η via transmission spectroscopy of a third type of device we fabricate within our platform, a waveguide-coupled photonic crystal (PhC) reflector. A schematic of the device is shown in Fig. 4a. The PhC is a ≈ 300 nm wide GaAs waveguide into which a periodic 1D array of elliptical holes is etched, with lattice constant a . Major and minor hole radii are kept constant over 19 lattice constants at the center, then reduced linearly over 5 constants at the two ends of the array (to minimize radiation losses). The false-color SEM in Fig. 4b illustrates the type of high resolution GaAs devices achievable within our platform. The periodic hole array defines a photonic bandgap for the TE-polarized GaAs mode on the left panel of Fig. 2a. The latter is strongly reflected by the PhC at bandgap wavelengths. Figure 4a describes the PhC reflector operation. Light is launched into the Si_3N_4 waveguide using a lensed optical fiber aligned to its cleaved facet, then transferred with efficiency η to the GaAs waveguide via the input mode transformer. At bandgap wavelengths, the GaAs-guided light is reflected with reflectivity R by the PhC, then transferred back into the Si_3N_4 waveguide via the input transformer, with efficiency η .

Simulated TE GaAs mode power transmission (T) and re-

flexion (R) spectra are shown in Fig. 4c, for PhCs with $a = 250$ nm and $a = 290$ nm and dimensions estimated by SEM from fabricated devices. Photonic bandgaps are evidenced by high reflectivity, high transmission extinction spectral regions marked in grey. We emphasize that R and T are spectra for the GaAs-confined modes, i.e., they do not include effects due to the mode transformers. We nevertheless observe, in Fig. 4d, similar features experimentally, which suggests spectrally broad mode transformer operation consistent with Fig. 2c. The experimental setup used is described in the Methods and SI. Room-temperature characterization is adequate to assess the low-temperature performance given the spectrally broadband nature of the elements involved and the expected thermo-optic shift of GaAs. Figure 4d shows normalized experimental TE-polarized transmission spectra for various fabricated devices with either $a = 250$ nm or $a = 290$ nm. Consistent spectral features achieved across many devices indicate that our photonic integration platform is scalable. Figure 4e shows a typical PhC reflectivity (R_{dev}) peak, obtained for one of the $a = 290$ nm devices, spectrally aligned with the transmission extinction region. The > 20 dB (≈ 25 dB at bandgap center) extinction highlighted in grey indicates highly efficient coupling from the Si_3N_4 access waveguide into the GaAs layer, since light not transferred to the GaAs is not reflected by the PhC. As described in the Methods, the photonic bandgap extinction can be used to obtain a lower bound for the mode transformer efficiency η . For a typically observed 20 dB extinction, $\eta > 90\%$, conservatively. For the peak extinction of ≈ 25 dB, $\eta > 94\%$.

To determine the external coupling efficiency η_{ext} , we took the transmitted power spectrum of a blank Si_3N_4 waveguide (i.e., with no GaAs devices) and normalized it by the supercontinuum source power spectrum. Assuming identical waveguide facets on both chip edges, $\eta_{\text{ext}} = 0.23 \pm 0.03$ over the 1100 nm to 1300 nm wavelength range, across three different devices (uncertainties are propagated single standard deviations. See SI for transmission spectra). To verify this, we estimated a mode-mismatch coupling efficiency $\eta_{\text{facet}} \approx 26\%$ between the Si_3N_4 waveguide mode and a Gaussian beam with $2.5\ \mu\text{m}$ diameter, consistent with the nominal lensed fiber spot-size diameter. The small difference between the experimental coupling efficiency and the calculated value suggests that propagation losses in the waveguide are relatively small.

Quantum dot coupling to waveguides in the heterogeneous platform

We next investigated QD emission coupling in our devices via photoluminescence (PL) measurements at cryogenic temperatures. In our setup, shown in Fig. S2 in the SI, devices were placed inside a liquid Helium flow cryostat, kept fixed on a copper mount connected to the cold finger. Testing temperatures ranged between 7 K and 30 K. A microscope system allowed individual devices to be visually located and optically pumped with laser light focused through a microscope objective. PL was collected by aligning a lensed fiber (mounted on a xyz nanopositioning stage inside the cryostat) to the corresponding Si_3N_4 waveguide facet. The collected PL was either sent to a grating spectrometer equipped with a liquid nitrogen cooled InGaAs detector array for spectrum mea-

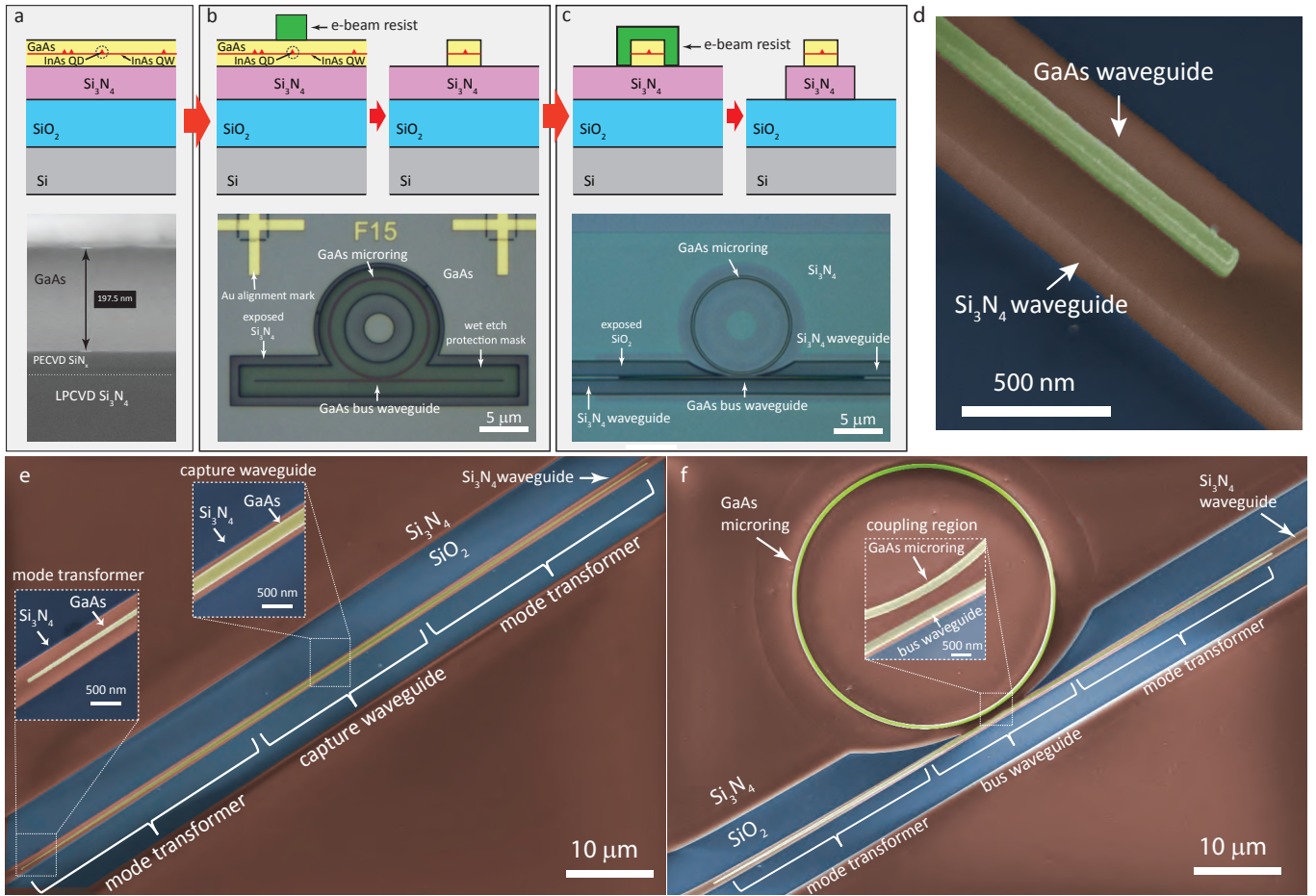


FIG. 3: Device fabrication. **a**, Top: schematic of bonded wafer stack used in fabrication, consisting of a top III-V layer, containing InAs QDs, that is directly bonded on top of a Si / $3 \mu\text{m}$ SiO_2 / 550 nm Si_3N_4 stack. Bottom: cross-sectional scanning electron micrograph (SEM) of bonded wafer stack. The $\approx 30 \text{ nm}$ SiN_x layer was grown on the GaAs wafer surface prior to bonding (see SI details). **b**, Top: GaAs device lithography and etching steps. Bottom: optical micrograph of etched GaAs microring resonator and bus waveguide. Au alignment marks used for registered electron-beam lithography are visible. A wet etch protection resist mask (not depicted in the schematic - see SI) is also visible. **c**, Top: Si_3N_4 waveguide lithography (aligned to the previously etched GaAs device) and etching steps. Bottom: optical micrograph of GaAs microring resonator and bus waveguide, and underlying Si_3N_4 waveguide. **d**, False-color SEM of tip of mode-transformer geometry, common to both devices in **e** and **f**. **e**, False-color SEM of fabricated GaAs waveguide (yellow) on top of Si_3N_4 (red) waveguide. Blue regions are exposed SiO_2 . Insets show details of the mode transformer end tip and the QD photon capture waveguide. **f**, False-color SEM of GaAs microring and bus waveguide, and underlying Si_3N_4 waveguide. Inset shows details of the microring-bus waveguide evanescent coupling region.

measurements, or towards a pair of amorphous WSi superconducting nanowire single-photon detectors (SNSPDs)²¹ for time-correlated single photon counting (TCSPC) measurements. We note that the high density QD population in our sample displayed a wide inhomogeneously broadened spectrum, with ensemble s-shell and p-shell peaks located approximately at 1100 nm and 1060 nm respectively.

We first investigated QD emission inside the basic hybrid device, a $\approx 300 \text{ nm}$ wide, $10 \mu\text{m}$ long GaAs waveguide with $20 \mu\text{m}$ long mode transformers, coupled to a 800 nm wide Si_3N_4 waveguide. Figure 5a shows the PL spectrum collected at a temperature of $\approx 7 \text{ K}$ for a device pumped at $\lambda = 1061 \text{ nm}$ (p-shell) with a tunable external-cavity diode laser (ECDL). Sharp spectral lines are excitonic complexes of individual QDs. A $\approx 700 \text{ pm}$ full-width at half-maximum

(FWHM) bandpass grating filter was used to spectrally isolate the line at 1130.18 nm in Fig. 5a, and a Hanbury-Brown and Twiss (HBT) setup was used to measure the autocorrelation $g^{(2)}(\tau)$, in Figs. 5b and 5c. The values $g^{(2)}(0) = 0.41 \pm 0.13$ obtained for the raw data, and $g^{(2)}(0) = 0 \pm 0.13$ obtained by taking into account the $\approx 129 \text{ ps}$ time resolution of our TCSPC system (see Methods), indicate that the QD in the GaAs device acts as source of single-photons that are directly launched into a Si_3N_4 waveguide. $g^{(2)}(0)$ uncertainties quoted here and below are 95 % fit confidence intervals (two standard deviations). Bunching at $\tau \approx \pm 2 \text{ ns}$ suggests QD blinking as observed with quasi-resonant (p-shell) excitation in ref. 47, and could be related to coupling of the radiative excited state to dark states. Our fits were done with a function that models coupling of a two-level system to a single dark state⁴⁸.

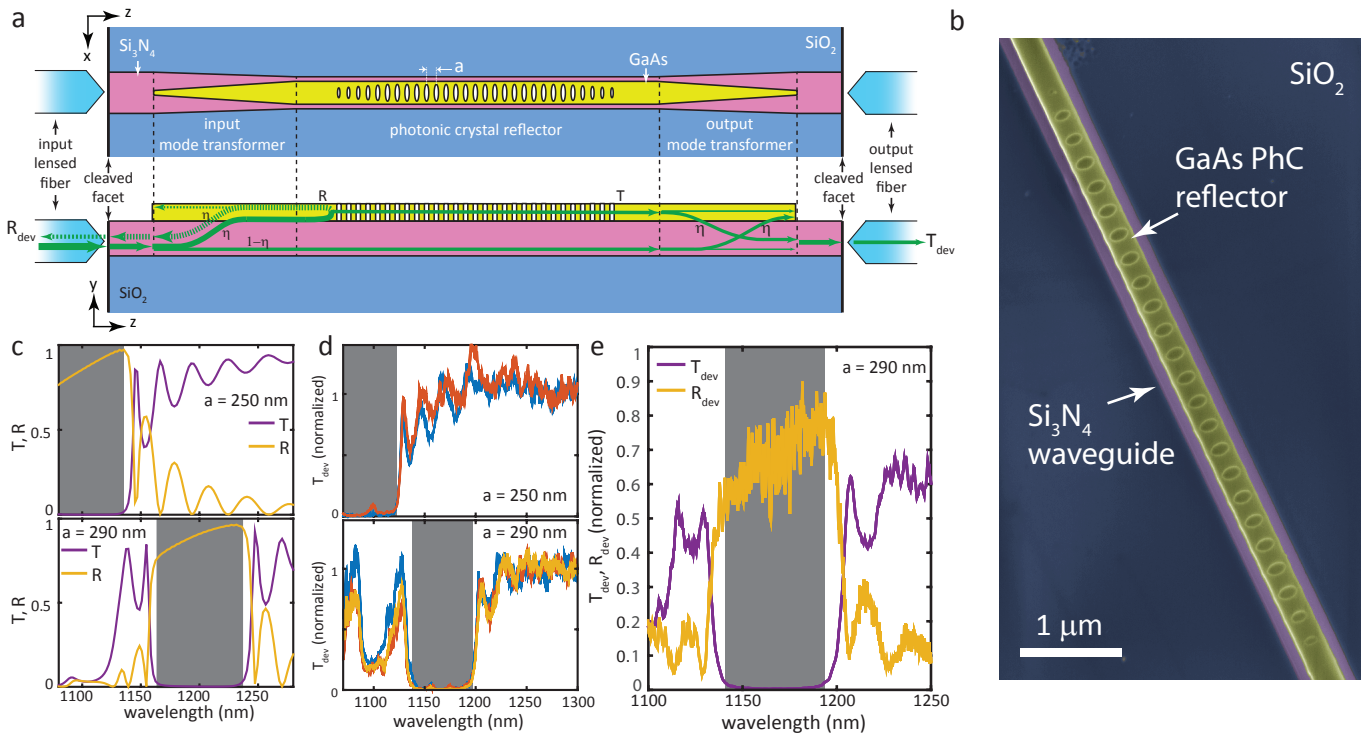


FIG. 4: **Characterizing mode transformer efficiency with a photonic crystal reflector.** **a**, Schematic of a PhC reflector device. Top: top-view. Bottom: cross-section. Green arrows indicate pathways taken by the optical signal injected at the input port. R and T stand for PhC modal power transmission and reflection spectra, and T_{dev} R_{dev} transmission and reflection spectra through the entire device, including lensed fibers. **b**, False-color SEM of fabricated GaAs PhC reflector (yellow) on top of a Si_3N_4 (pink) waveguide, on top of exposed SiO_2 (blue). **c**, FDTD-simulated TE modal transmission (T, purple) and reflection (R, yellow) spectra as a function of wavelength for the PhC (without mode transformers), for two different lattice constants a . **d**, Experimental transmission spectra for various PhC reflectors with $a = 250$ nm (top) and $a = 290$ nm (bottom), normalized first by the transmission spectrum of a baseline Si_3N_4 waveguide (without GaAs sections), then to the mean transmission at wavelengths between 1250 nm and 1300 nm. Different colors indicate different devices. **e**, Experimental transmission and reflection spectra for a PhC reflector with $a = 290$ nm, normalized to the transmission spectrum of a baseline Si_3N_4 waveguide (SI for details). Grey areas have transmission < -15 dB in **c-d**, < -20 dB in **e**.

Lifetime measurements for the same QD line were next performed by modulating the ECDL pump light with an electro-optic modulator (see Methods and SI). The decay curves show in Fig. 5d were fitted with a single exponential function, revealing a lifetime $\tau_{\text{sp}} = 1.014 \text{ ns} \pm 0.004 \text{ ns}$ (lifetime uncertainties here and below are from the fit and correspond to one standard deviation). Assuming a fiber-to-chip coupling efficiency of 22 %, and a coupler efficiency $\eta = 98$ %, we estimate a QD-waveguide coupling parameter $\beta = 0.20 \pm 0.07$ (uncertainty from propagated errors in the optical characterization of the measurement system, corresponding to one standard deviation. See Methods for details). This value, though appreciable, is less than the theoretical maximum of 0.37. This discrepancy could be attributed to non-optimal QD position and electric dipole moment orientation.

Weak-coupling cavity QED in the heterogeneous platform

We next investigated cavity effects on the radiative rate of single QDs coupled to whispering gallery modes (WGMs) of GaAs microring resonators (Fig. 3f). The devices consisted of 20- μm diameter microrings formed by ≈ 300 nm wide waveguides, evanescently coupled to ≈ 300 nm wide GaAs

bus waveguides spaced by gaps of varying dimensions. In this scheme, light from QDs inside the ring is outcoupled through the bus waveguide and then transferred to the Si_3N_4 waveguide via the mode transformers. Figure 6a shows PL spectra for three different resonators, with coupling gaps of 150 nm, 250 nm and 350 nm, pumped at high intensities with 975 nm laser light (resonant with the quantum well transitions). Peaks are PL from the QD ensemble coupled to WGMs. Quality factors for devices with the gap spacings of 150 nm, 250 nm and 350 nm are 2.5×10^3 , 6×10^3 and 2×10^4 . The increased Q for larger gaps is due to a decreased cavity-bus waveguide coupling, indicating that the geometrical control afforded by our fabrication platform enables fine control of cavity outcoupling rates. Pumping one of the $Q \approx 1.1 \times 10^4$ microresonators at 1058 nm (p-shell) allowed observation of the single QD excitonic line at 1125.92 nm in Fig. 6b, which was coupled to one of the cavity's WGMs. Background emission, likely from other QDs and (multi)excitonic complexes in the active material, is also observed in the different WGMs. Figure 6c indicates the cavity-coupled QD acts as a single-photon source with $g^{(2)}(0) = 0.28 \pm 0.01$ ($g^{(2)}(0) = 0.07 \pm 0.01$ adjusted for detection time resolution).

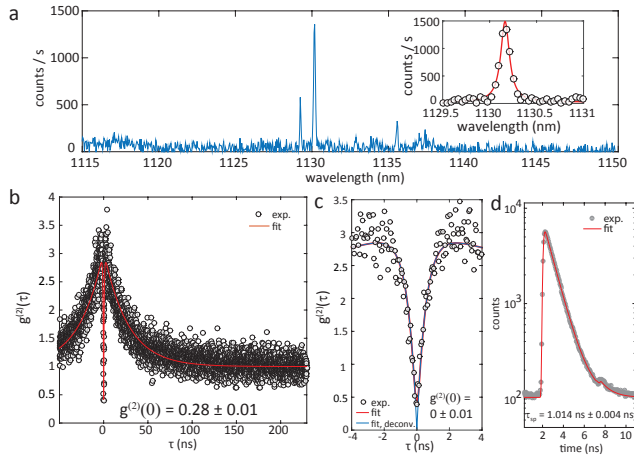


FIG. 5: Quantum dot-waveguide coupling. **a**, Photoluminescence spectrum for a single QD inside a GaAs waveguide as in Fig. 3e, pumped with 1061 nm wavelength laser light. The PL is transferred to the bottom Si_3N_4 waveguide, and collected with a lensed optical fiber inside of a Liquid Helium flow cryostat (see SI for experimental details). Sharp lines are exciton transitions from a single QD. Inset: Fit of PL peak at 1130.18 nm. **b**, Second-order correlation as a function of time delay τ for the 1130.18 nm line. Circles mark experimental data, red line is a fit (see Methods and SI). **c**, Zoom-in of **b** near $\tau = 0$. The blue curve and quoted $g^{(2)}(0)$ are obtained from the red fit by deconvolving the detection time-response. Uncertainties for $g^{(2)}(0)$ are 95 % fit confidence intervals (two standard deviations). **d**, Photoluminescence decay trace for the 1130.18 nm line. Gray dots are experimental data, the red line is a fit with a monoexponential function with lifetime τ_{sp} . The uncertainty is obtained from the fit and corresponds to a single standard deviation.

We next demonstrated tunable control of Purcell radiative rate enhancement in a device with $Q \approx 2.3 \times 10^4$, at a fixed temperature of ≈ 7 K. Pumping at $\lambda = 1065$ nm (p-shell) allowed us to observe the cavity-mode-coupled single QD exciton line X_1 in Fig. 6d, as well as a cavity-detuned exciton X_2 . For the X_1 line, as seen in Fig. 6e, $g^{(2)}(0) = 0.72 \pm 0.08 > 0.5$ ($g^{(2)}(0) = 0.52 \pm 0.08$ adjusted for detection time resolution), due to background emission from the cavity mode, which was transmitted by the band-pass filter introduced before detection. Indeed, based on the fit shown in Fig. 6d, cavity emission corresponds to $\approx 45\%$ of the filtered light intensity. To tune the cavity with respect to the QD exciton, we used the nitrogen gas-tuning mechanism of ref. 49. A small amount of gaseous N_2 is introduced in steps into the cryostat, and gettering at the GaAs surfaces red-shifts the cavity resonance by a small amount at each step. This is observed in the left panel in Fig. 6f, where the PL spectrum of the cavity-coupled QD exciton (X_1) is seen to grow in intensity as its spectral (wavelength) detuning Δ from the cavity center tends to zero. The variation in intensity comes together with a variation in the exciton lifetime, evident in the corresponding decay curves on the right panel of Fig. 6f. Biexponential fits to the decay data (monoexponential for $\Delta \approx 0.53$ nm and $\Delta \approx 0.84$ nm) are also shown. The detuning-dependent variations in X_1 intensity and decay lifetime are summarized respectively in the

left and right panels in Fig. 6g, evidencing high-resolution, strong control of the exciton radiative rate via cavity coupling achieved in our platform. Further details on PL spectrum and decay fitting and assignment of lifetimes are given in the SI. Comparing with the ≈ 1 ns lifetime in the waveguide, we can extract a maximum radiative rate enhancement factor of ≈ 4 for the QD. From the calculated WGM mode volume $V_{\text{eff}} = 75.5(\lambda/n_{\text{GaAs}})^3$ (n_{GaAs} is the GaAs refractive index) and the experimental $Q = 2.3 \times 10^4$, we expect a maximum Purcell Factor $F_p \approx 23$ (see Methods). The lower Purcell factor observed in experiment could be due to non-optimal spatial location and polarization alignment of the QD with respect to the microring mode.

Discussion The results presented demonstrate that our platform enables the creation of integrated photonic circuits that incorporate quantum-dot based devices with complex geometries. As discussed above and in the SI, further improvements to the single-photon capture efficiency (quantified by the β -factor) can be achieved through optimized wafer stacks (both Si_3N_4 and the GaAs epi-stack) and device geometries. In particular, our platform allows the creation of geometries providing high Purcell radiative rate enhancement where high β may be achieved, such as microdisk, microring or photonic crystal-based cavities and slow-light waveguides. The high reflectivity achieved with our PhC reflectors furthermore suggests a path forward towards unidirectional QD emission in a waveguide. Alternatively, chiral coupling to waveguide modes³⁷ could also be explored. Strongly-coupled QD-cavity systems^{8,12,27} evanescently coupled to a bus waveguide could also be envisioned in our platform.

As mentioned above, our III-V wafers contained a high density of QDs ($> 100/\mu\text{m}^2$), randomly distributed across the wafer surface, which led to the deterioration of the purity of our on-chip single-photon sources. It is also possible that the pronounced blinking observed in the autocorrelation traces might stem from interactions between many neighboring QDs. Low-density QD growth constitutes a clear way forward here. In this case, QD positioning techniques such as the one developed in ref. 13 -a technique fully compatible with our fabrication process- become essential. Precise quantum dot location within a nanophotonic structure would also allow β and Purcell factor optimization.

The underlying Si_3N_4 waveguides demonstrated here provide not only a way to route single-photons with low loss across the chip, but also a means to explore nonlinear optical processes with single photons. For instance, four-wave-mixing-based wavelength conversion of single-photon-level laser light was recently demonstrated in a Si_3N_4 microring resonator with cross-sectional dimensions similar to those of our waveguides, and fabricated with the same etch process⁷. This means that the required dispersion profiles and nonlinear coefficients are attainable within our platform. At the same time, passive structures with cross-sections optimized for low propagation losses may also be implemented, for instance with thinner Si_3N_4 (see SI) and potentially even with a top oxide cladding. The introduction of elements such as on-chip delay lines, high quality Si_3N_4 -based filters, and mi-

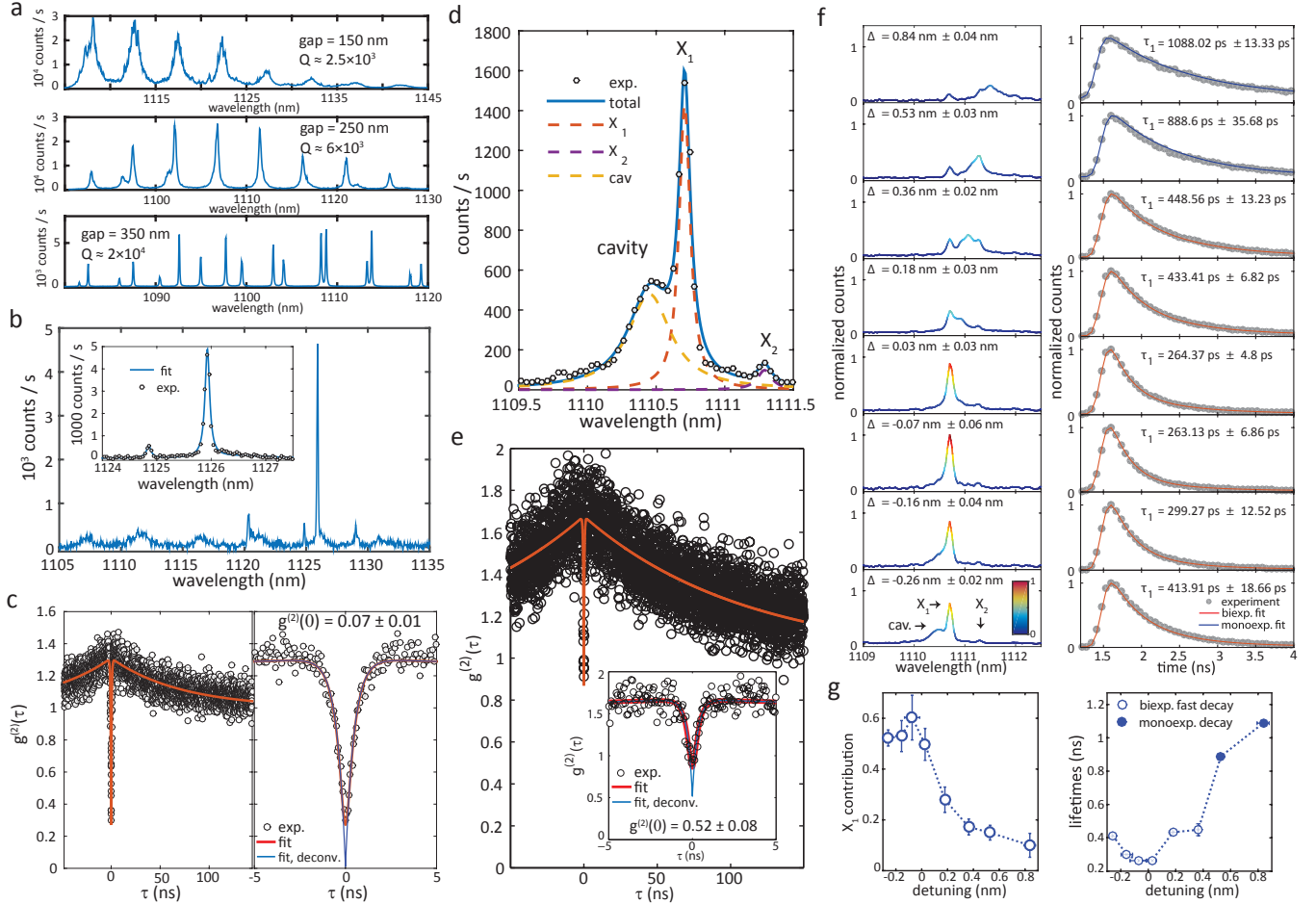


FIG. 6: Quantum dot-cavity coupling. **a**, Photoluminescence (PL) spectra as a function of wavelength from a QD ensemble pumped with laser light at 975 nm, emitting inside three different GaAs microring resonators. Peaks are whispering-gallery modes (WGMs) with quality factor Q , which increases with the microring-bus waveguide gap width. **b**, PL spectrum for a single QD coupled to a $Q \approx 1.1 \times 10^4$ WGM. Inset: fit of cavity-coupled QD emission near 1126 nm. **c**, Left: second-order correlation $g^{(2)}(\tau)$ for the 1126 nm exciton line in **b**. Right: close-up near $\tau = 0$. Circles are experimental data, red lines are a fit. The blue curve and quoted $g^{(2)}(0)$ are obtained from the red fit by deconvolving the detection time-response. **d**, PL spectrum for a single QD in a microring, coupled to a $Q \approx 2.3 \times 10^4$ WGM. Circles: experimental data. Blue continuous line: fit. Dashed lines: fitting Lorentzians for the cavity and two excitons, X_1 and X_2 . **e**, $g^{(2)}(\tau)$ for X_1 in **d**. Inset: close-up near $\tau = 0$. **f**, Left panel: PL spectra for varying spectral detuning Δ between X_1 and the cavity. Δ is obtained from fits as in **d**. All spectra are normalized to the intensity maximum at $\Delta \approx -0.07$ nm. The color scale indicates normalized intensity. Right panel: corresponding X_1 photoluminescence decay curves. Grey dots are experimental data, red (blue) lines are biexponential (monoexponential) decay fits. For biexponential fits, τ_1 is the fast lifetime. **g**, Left panel: integrated intensity as a function of Δ for the filtered X_1 exciton contribution to the the PL spectra in **f**, obtained from Lorentzian fits as in **d**, normalized by the integrated intensity of the full fitted spectrum. Right panel: decay lifetimes for the fits in **f**, as a function of Δ . Open blue circles are the fast biexponential decay lifetimes, closed blue circles are the monoexponential decay lifetimes. Uncertainties for $g^{(2)}(0)$, Δ and the X_1 magnitude are 95 % fit confidence intervals (two standard deviations). Lifetime uncertainties are single standard deviations from the exponential decay fits.

cropping add-drops, can also be envisioned.

Our platform is also amenable to further integration with waveguide-based superconducting nanowire single-photon detectors⁵⁰. Finally, the fabrication process can be adapted for materials such as AlN and LiNbO₃, which may enable active electro-optic phase control. We anticipate all of these features will enable a new class of monolithic on-chip devices comprising emission, routing, modulation and detection of quantum light.

Methods

Numerical simulation Calculations of waveguide β -factors is done with finite-difference time-domain simulations. We simulate a x -oriented electric dipole source radiating inside the GaAs ridge of the stacked GaAs/Si₃N₄ waveguide structure shown in Fig. 1d. The simulation is 3D, and the coupled waveguide structure length is 1 μ m. Perfectly-matched layers are used to emulate either open regions (air and SiO₂ semi-infinite spaces above and below the geometry), or infinite waveguides (in the planes perpendicular to x and y). We obtain the steady-state electromagnetic fields at the six boundaries of the simulation window, and compute the total emitted power P by integrating the steady-state Poynting vector through them. At the $\pm z$

and $-z$ planes, we calculate overlap integrals of the radiated field with the field of the fundamental TE GaAs mode (Fig. 2a left panel, at $\lambda = 1100$ nm). This allows us to determine β , the fraction of the total emitted power that is carried through the $\pm z$ planes by the GaAs mode.

The mode transformer simulations are also performed with FDTD. We launch the fundamental TE GaAs mode of the waveguide structure in Fig. 1d, shown in the left panel of Fig. 2a, into the mode transformer, at the $z = 0$ plane. We obtain the steady-state electromagnetic fields at the output ($z = 20 \mu\text{m}$) plane on the mode transformer, and calculate the overlap integral between this and the output Si_3N_4 mode (right panel on Fig. 2a). Dividing it by the launched input power we obtain the mode transformer coupling efficiency η .

We proceed similarly for the simulation of modal reflectivity and transmissivity for the photonic crystal reflector of Fig. 4a. For reflectivity, we place a field monitor at the $z = 0$ plane, and the source at $z = 100$ nm.

To determine the mode volume V_{eff} used in the Purcell factor estimate, we use $V_{eff} = \int_V dV \epsilon(\mathbf{r}) |\mathbf{E}(\mathbf{r})|^2 / \max \{ \epsilon(\mathbf{r}) |\mathbf{E}(\mathbf{r})|^2 \}$, where the volume integral is evaluated over the entire microring resonator. Because the ring radius is large ($R = 10 \mu\text{m}$), we assume the whispering gallery mode fields across the microring cross-section have the same distribution as the fundamental TE GaAs mode of Fig. 2a's left panel, and an azimuthal dependence $\exp(i \cdot m\phi)$. Then, $V_{eff} = 2\pi \cdot R \cdot \int_A dA \epsilon(\mathbf{r}) |\mathbf{E}(\mathbf{r})|^2 / \max \{ \epsilon(\mathbf{r}) |\mathbf{E}(\mathbf{r})|^2 \}$, where A is the cross-sectional waveguide area. The maximum Purcell factor (assuming spatial and polarization alignment of the dipole) is calculated with the expression $F_p = (3/4\pi^2) \cdot Q/V_{eff}'$, where V_{eff}' is the mode volume in cubic wavelength in the GaAs.

Experimental determination of mode transformer coupling efficiency Power transmission and reflection spectra T_{dev} and R_{dev} are determined experimentally using the setup in Fig. S1a of the SI. Light from a fiber-coupled supercontinuum laser source is passed through a 3 dB fiber directional coupler and polarization controller, then launched into the input waveguide with a lensed fiber. Transmitted light is collected with another lensed fiber aligned to the output waveguide facet at the opposite edge of the chip, and sent to an optical spectrum analyzer (OSA). Reflected light is captured by the input fiber, and routed to the OSA via the 3 dB splitter.

To estimate a lower bound for η , we use a simple model to obtain an expression for the transmitted power at the output, T_{dev} , as suggested in Fig. 4a. Light launched at the input Si_3N_4 waveguide is transferred with efficiency η into the GaAs guide, whereas a residual $(1 - \eta)$ portion of the original power remains in the Si_3N_4 guide. Light transferred to the GaAs guide will be reflected with a reflectivity R by the PhC, and transmitted through it with transmissivity T . The output mode transformer converts light transmitted through the PhC reflector back into the Si_3N_4 guide, with efficiency η . We assume that the residual light that remains in the Si_3N_4 after the input mode transformer is unaffected by the PhC, after which it is partially transferred with efficiency η to the GaAs guide by the output mode converter, and is then lost as radiation at the terminated GaAs structure tip. Light collected by the output lensed fiber thus has two components, one that remains in the Si_3N_4 guide, and one that is transferred to and from the GaAs guide, and interacts with the PhC reflector. The maximum power collected by the output lensed fiber is T_{dev} , with

$$T_{dev} \leq \eta_{ext} \left[\eta^2 T + (1 - \eta)^2 + 2 \cdot \eta(1 - \eta)\sqrt{T} \right]. \quad (1)$$

Inside the square brackets, the first and second terms correspond respectively to light transmitted through the PhC and residual light that

remains in the Si_3N_4 guide, and the third term comes from the interference between the two. The transmitted power for wavelengths in and out of the bandgap region are $T_{dev,in}$ and $T_{dev,out}$, respectively, and we define the extinction ratio $\alpha = \frac{T_{dev,in}}{T_{dev,out}}$. Because experimentally $T_{dev,in}$ is at least one order of magnitude lower than $T_{dev,out}$, we can assume that the PhC transmission at bandgap wavelengths is negligible, so that $T \approx 0$ and

$$\alpha > \frac{(1 - \eta)^2}{\eta^2 T + (1 - \eta)^2 \pm 2 \cdot \eta(1 - \eta)\sqrt{T}} > \frac{(1 - \eta)^2}{\eta^2 + (1 - \eta)^2 + 2 \cdot \eta(1 - \eta)} \quad (2)$$

Isolating η , we obtain the inequality $\eta^2 + (2 - \alpha)/(\alpha - 1) + 1 < 0$. The minimum root of the quadratic equation is our lower bound for η . For $\alpha = -20$ dB, as typically observed in our PhC spectra, $\eta > 90\%$, conservatively. For the peak extinction of ≈ 25 dB, $\eta > 94\%$.

Experimental determination of external coupling efficiency The external coupling efficiency η_{ext} includes the chip-to-fiber coupling efficiency and propagation losses in the Si_3N_4 waveguide leading to the device. We employ the setup of Fig. S1a of the SI to obtain the transmitted power spectrum of a blank Si_3N_4 waveguide (i.e., with no GaAs devices). Prior to this measurement, the polarization of the incident light is set to TE by probing a PhC reflector and minimizing the transmitted power over the photonic bandgap with the polarization controller. The lensed fibers are then aligned to the blank Si_3N_4 waveguide, and the transmission spectrum is recorded. The spectrum is then normalized by the supercontinuum source power spectrum, obtained by bypassing the lensed fibers and the device. The resulting transfer function accounts for insertion losses through the two lensed fibers ($\approx 31\%$), and through the device, $IL_{dev} = \eta_{dev}^{-1} = (\eta_{ext,in} \cdot \eta_{ext,out})^{-1}$. Assuming that the waveguide facets are identical on both edges of the chip, $\eta_{ext,in} = \eta_{ext,out} = \eta_{ext}$, the external coupling efficiency is $\eta_{ext} = \sqrt{\eta_{dev}}$. Figure S1b in the SI shows the average measured η_{ext} for 3 different waveguides as a function of wavelength (the red curve and grey area correspond to the mean and standard deviation over the three measurements, respectively). Averaging this curve across the 1100 nm to 1300 nm wavelength range produces $\eta_{ext} = 0.23 \pm 0.03$ (the uncertainty is obtained by propagating the standard deviations from the three devices). The theoretical mode-mismatch coupling efficiency is calculated with the overlap integral

$$\eta_{facet} = \frac{\text{Re} \left\{ \iint_S (\mathbf{e}_f \times \mathbf{h}^*) \cdot \hat{z} dS \iint_S (\mathbf{e} \times \mathbf{h}_f^*) \cdot \hat{z} dS \right\}}{\text{Re} \left\{ \iint_S (\mathbf{e}_f \times \mathbf{h}_f^*) \cdot \hat{z} dS \right\} \text{Re} \left\{ \iint_S (\mathbf{e} \times \mathbf{h}^*) \cdot \hat{z} dS \right\}} \quad (3)$$

taken over the cross-sectional area S of the input/output Si_3N_4 waveguide. Here, \mathbf{e} and \mathbf{h} are the electric and magnetic field components of the fundamental TE Si_3N_4 input/output waveguide mode (right panel on Fig. 2a), and \mathbf{e}_f and \mathbf{h}_f are the field components of a focused Gaussian beam with a spot size of $2.5 \mu\text{m}$. The Gaussian beam spot size is consistent with specifications from the lensed fiber manufacturer. With eq.(3), we obtain $\eta_{facet} \approx 26\%$ for a 580 nm thick \times 800 nm wide Si_3N_4 waveguide, at a wavelength of 1110 nm.

Second-order correlation measurements and fits A Hanbury-Brown and Twiss (HBT) setup was used to obtain the second-order correlation function $g^{(2)}(\tau)$ of QD emission upon continuous-wave pumping. In our experiments, histograms of delays between detection events in the two single-photon detectors were measured. We related these histograms to $g^{(2)}(\tau)$ as explained below. We first calculated delay probability distributions $C(\tau)$ by normalizing the delay histograms. Sufficiently far away from zero time delay, $C(\tau) \approx A \exp(-A\tau)$. We took the 1000 longest-delay bins of our histograms and perform a log-log linear fit to obtain A . The histograms

were then normalized by A . For $\tau \approx 0$, $g^{(2)}(\tau) \approx C(\tau)$ (see ref. 51). The $g^{(2)}(\tau)$ data was modeled with the double-exponential function

$$g^{(2)}(\tau) = 1 + A_1 \exp(\lambda_1 \cdot \tau) + A_2 \exp(\lambda_2 \cdot \tau), \quad (4)$$

with $A_1 + A_2 = -1$. This functional form is expected from a two-level system coupled to a single dark state⁴⁸, and describes both antibunching at $\tau = 0$, bunching at some later time delay, and a return to the Poissonian level at $\tau \rightarrow \infty$. To take into account the $\sigma \approx 129$ ps time-response of detection system (see below for details), we convolved the $g^{(2)}(\tau)$ above with a Normal distribution function $N(\tau, \sigma)$:

$$g_C^{(2)}(\tau) = g^{(2)}(\tau) * N(\tau, \sigma) = 1 + A_1 E_1(\tau) + A_2 E_2(\tau), \quad (5)$$

where

$$E_n(\tau) = \frac{\lambda_n}{2} \exp\left(\frac{\lambda_n \sigma}{2}\right) \left\{ \operatorname{erf}\left(-\frac{\tau}{\sqrt{2}\sigma} + \frac{\lambda_n \sigma}{\sqrt{2}}\right) e^{-\lambda_n \tau} + \operatorname{erf}\left(\frac{\tau}{\sqrt{2}\sigma} + \frac{\lambda_n \sigma}{\sqrt{2}}\right) e^{\lambda_n \tau} \right\} \quad (6)$$

and $n = 1, 2$. Finally, to account for a Poissonian background, we used⁵¹

$$g_{C,B}^{(2)}(\tau) = 1 + \frac{1}{(1+b)^2} [g_C^{(2)}(\tau)]. \quad (7)$$

The fits shown in the main text were done using $g_{C,B}^{(2)}(\tau)$ above, through a nonlinear least-squares procedure. For the QD in a waveguide of Figs. 5b and 5c, the background b was used as a fit parameter, while for the cavity-coupled QDs of Figs. 6c and 6e, b was fixed at values estimated from fits to emission spectra (see below for spectrum fitting procedures). To plot $g^{(2)}(\tau)$ without the effect of the finite timing resolution, we used $\sigma = 0$ in eq.(6) and used the same fitting parameters. Uncertainties quoted for $g^{(2)}(0)$ are 95 % fit confidence intervals, corresponding to 2 standard deviations.

Photoluminescence spectrum fits The photoluminescence spectra in Figs. 6b and 6f were fitted with a sum of three Lorentzians, representing the cavity and two excitons, X_1 and X_2 . A representative fitted spectrum is shown in Fig. 6d, where the individual contributions are also displayed. To produce the left panel on Fig. 6g, the different contributions were multiplied by a spectrum representing the bandpass grating filter used experimentally, and the X_1 contribution was then normalized to the sum of the integrated intensities of all components before filtering. The wavelength detuning Δ between X_1 and the cavity was determined from these fits. All uncertainties quoted for Δ and the X_1 , X_2 and cavity contributions correspond to 95 % fit confidence intervals (two standard deviations).

Photoluminescence decay measurements For excited state lifetime measurements, we employed a 10 GHz lithium niobate electro-optic modulator (EOM) to produce a 80 MHz, ≈ 200 ps pulse train from the CW ECDL laser. A fiber-based polarization controller (FPC) was used to control the polarization of the ECDL light going into the EOM, and a DC bias was applied to the EOM to maximize signal extinction. An electrical pulse source was used to produce an 80 MHz train of ≈ 200 ps pulses of < 1 V peak amplitude, which was then amplified and used to drive the EOM via its radio frequency (RF) port. A trigger signal from the pulse generator served as the reference channel in our TCSPC system. Figure S3a in the SI shows a typical temporal profile for the pulses produced by the EOM, detected with an SNSPD. Pulse FWHM of ≈ 200 ps and > 20 dB extinction are observed. The pulsed electrical signal produced small satellite peaks that were imprinted in the optical signal, as indicated in Fig. S3a. These satellite peaks typically appeared a few ns after each proper pulse, and were ≈ 20 dB below the latter in intensity. Impulse response functions (IRFs) such as the one in Fig. S3a were

used in decay lifetime fits as explained below, so that the effect of satellite peaks, though minimal, was accounted for. Lastly, to determine the time resolution of our detection system, we launched attenuated few-picosecond pulses from a Ti:Sapphire mode-locked laser at 975 nm into the SNSPDs, to obtain the temporal trace in Fig. S3b. The peak can be well fitted with a Gaussian with standard deviation $\sigma = 129$ ps ± 0.04 ps (uncertainty is a 95 % least-squares fit confidence interval, corresponding to two standard deviations).

Photoluminescence decay fits Quantum dot emission decay fits were performed using maximum likelihood estimation. We consider a lifetime trace $Y^k = \{Y_i\}_{i=1}^k$ where a known number of photon counts N is distributed over k time bins, such that the bin counts y_i follow a multinomial distribution²³. The maximum likelihood estimator is

$$g_{MLE}(y^k) = \arg \min_{\theta \in \Theta} \left\{ - \sum_{i=1}^k y_i \ln p_i(\theta) \right\}, \quad (8)$$

where θ is a vector in the multidimensional parameter space Θ . Estimates for the various fit parameters are obtained by finding θ that minimizes the expression in the curly brackets, where y_i is the i -th bin count, and $p_i(\theta)$ is a probability density function that models the decay, evaluated at the i -th bin. We define $p_i(\tau) = e^{-ir/k} \frac{e^{\hat{k}} - 1}{1 - e^{-r}}$,

with $r \triangleq \frac{i \cdot \Delta t}{\tau}$. For a monoexponential decay when a portion b of the signal is due to background emission,

$$p_i(\theta) = p_i(\tau, b) = \frac{b}{k} + (1-b)p_i(\tau) \quad (9)$$

For biexponential decay with a background b , let $\tau \triangleq (\tau_1, \tau_2)^T$. Then $p_i(\tau, a, b)$ (where a is the contribution of the first exponential decay) may be expressed as

$$p_i(\theta) = p_i(\tau, b, a) = \frac{b}{k} + (1-b)[ap_i(\tau_1) + (1-a)p_i(\tau_2)] \quad (10)$$

Variances for the estimated parameters in θ can be obtained from the diagonal elements of the inverse of the Fisher Information Matrix (see SI for further details). In the fitting procedure, the trial decay function $p_i(\theta)$ is numerically convolved with the experimentally measured, background-subtracted impulse response function (IRF) and used in eq.(8). Because the optical pulses used to obtain the IRF follow a considerably different path length towards the detector than the QD signal, the IRF and QD decay traces are delayed with respect to each other. We manually align the two traces to minimize fit residuals. Uncertainties given in the text correspond to standard deviations for the various parameters, obtained from the diagonal elements of the inverse of the Fisher information matrix computed with the expectation values from the fit (corresponding to the Cramér-Rao lower bound).

Estimate of β Below we estimate the coupling β of the QD exciton at $\lambda \approx 1330.18$ nm of Fig. 5a into the guided TE mode of the GaAs waveguide where it was hosted. Ideally such a measurement would involve saturating the QD under pulsed excitation, where the maximum possible photon flux from the QD is given by the laser repetition rate. Because a pulsed source with sufficient power to saturate the QD was unavailable, our estimate relied on the continuous-wave emission spectrum of Fig. 4a. A three-level system model for the QD was then used to account for blinking. First, we measured the spectrum of a laser signal of known power at 1070 nm with our spectrometer, using the same fiber-coupled input as that for Fig. 5a. The laser was attenuated with a calibrated variable optical attenuator (VOA), and launched into a fiber-based 10:90 power splitter (with a calibrated power-splitting ratio), the 90 % port of which was sent to

a photodiode for power monitoring. Integration of the background-subtracted laser spectrum counts divided by the laser power gave a factor of 0.0023 counts per photon at the spectrometer fiber-coupled input (this includes losses at the fiber connector, spectrometer slit, grating and output slit before the InGaAs detector array). This allowed us to obtain, from the fitted QD spectrum of Fig. 5a, a photon flux $P = 3.0 \times 10^6 \text{ s}^{-1} \pm 0.5 \times 10^6 \text{ s}^{-1}$ (errors come from the 95 % fit confidence intervals) at this fiber input for the 1130.18 nm exciton line (accounting for the wavelength difference). We next expanded the photon flux as $P = X\beta\eta\eta_{\text{ext}}\eta_{\text{TF}}$, where X is the exciton population probability, η the mode transformer efficiency, η_{ext} the lensed fiber-to-chip coupling efficiency, and $\eta_{\text{TF}} = 0.91 \pm 0.03$ is the lensed fiber transmission (uncertainty from measurement error, correspond-

ing to one standard deviation). Solving the three-level system rate equations (with one bright and one dark transition) that fit the $g^{(2)}(\tau)$ data in Fig. 4c - assuming the lifetime in Fig. 4d for the bright transition - we obtain $X = 0.15 \pm 0.04$, where the uncertainty is the 95 % fit confidence interval. We note that connecting the dark state to either the ground or bright excited state in our model leads to $X \approx 0.15$. Assuming $\eta = 98 \%$ (the maximum from simulation) and $\eta_{\text{ext}} = 0.22$, a reasonable value from Fig. S1b at 1130 nm, we obtain, propagating uncertainties, $\beta = 0.20 \pm 0.07$.

Acknowledgements We thank Daron Westly and Rob Ilic from the NIST CNST for invaluable aid with fabrication. J.L. acknowledges support under the Cooperative Research Agreement between the University of Maryland and NIST-CNST, Award 70NANB10H193.

-
- * Electronic address: marcelo.davanco@nist.gov
 † Electronic address: liujin23@mail.sysu.edu.cn
 ‡ Electronic address: kartik.srinivasan@nist.gov
- 1 A. Politi, M. J. Cryan, J. G. Rarity, S. Yu, and J. L. O'Brien, "Silica-on-Silicon Waveguide Quantum Circuits," *Science* **320**, 646– (2008).
 - 2 S. Tanzilli, A. Martin, F. Kaiser, M. De Micheli, O. Alibart, and D. Ostrowsky, "On the genesis and evolution of Integrated Quantum Optics," *Laser & Photonics Reviews* **6**, 115–143 (2012).
 - 3 T. C. Ralph, "Quantum computation: Boson sampling on a chip," *Nature Photonics* **7**, 514–515 (2013).
 - 4 J. C. Loredo, M. A. Broome, P. Hilaire, O. Gazzano, I. Sagnes, A. Lemaitre, M. P. Almeida, P. Senellart, and A. G. White, "BosonSampling with single-photon Fock states from a bright solid-state source," arXiv preprint arXiv:1603.00054 (2016).
 - 5 F. Marsili, V. B. Verma, J. A. Stern, S. Harrington, A. E. Lita, T. Gerrits, I. Vayshenker, B. Baek, M. D. Shaw, R. P. Mirin, and S. W. Nam, "Detecting single infrared photons with 93% system efficiency," *Nature Photonics* **7**, 210–214 (2013).
 - 6 Q. Li, M. Davanço, and K. Srinivasan, "Efficient and low-noise single-photon-level frequency conversion interfaces using silicon nanophotonics," *Nat Photon* **10**, 406–414 (2016).
 - 7 R. Riedinger, S. Hong, R. A. Norte, J. A. Slater, J. Shang, A. G. Krause, V. Anant, M. Aspelmeyer, and S. Gröblacher, "Non-classical correlations between single photons and phonons from a mechanical oscillator," *Nature* **530**, 313–316 (2016).
 - 8 S. Sun, H. Kim, G. S. Solomon, and E. Waks, "A quantum phase switch between a single solid-state spin and a photon," *Nature Nanotechnology* **11**, 539–544 (2016).
 - 9 A. J. Bennett, J. P. Lee, D. J. P. Ellis, I. Farrer, D. A. Ritchie, and A. J. Shields, "A semiconductor photon-sorter," *Nature Nanotechnology* **11**, 857–860 (2016).
 - 10 A. Maser, B. Gmeiner, T. Utikal, S. Gtzinger, and V. Sandoghdar, "Few-photon coherent nonlinear optics with a single molecule," *Nature Photonics* **10**, 450–453 (2016).
 - 11 A. Reinhard, T. Volz, M. Winger, A. Badolato, K. J. Hennessy, E. L. Hu, and A. Imamolu, "Strongly correlated photons on a chip," *Nature Photonics* **6**, 93–96 (2012).
 - 12 I. Fushman, D. Englund, A. Faraon, N. Stoltz, P. Petroff, and J. Vučković, "Controlled Phase Shifts with a Single Quantum Dot," *Science* **320**, 769–772 (2008).
 - 13 N. Somaschi, V. Giesz, L. De Santis, J. C. Loredo, M. P. Almeida, G. Hornecker, S. L. Portalupi, T. Grange, C. Antn, J. Demory, C. Gmez, I. Sagnes, N. D. Lanzillotti-Kimura, A. Lematre, A. Auffeves, A. G. White, L. Lanco, and P. Senellart, "Near-optimal single-photon sources in the solid state," *Nature Photonics* **10**, 340–345 (2016).
 - 14 X. Ding, Y. He, Z.-C. Duan, N. Gregersen, M.-C. Chen, S. Unsleber, S. Maier, C. Schneider, M. Kamp, S. Hfing, C.-Y. Lu, and J.-W. Pan, "On-Demand Single Photons with High Extraction Efficiency and Near-Unity Indistinguishability from a Resonantly Driven Quantum Dot in a Micropillar," *Physical Review Letters* **116**, 020401 (2016).
 - 15 J. Cardenas, C. B. Poitras, K. Luke, L. W. Luo, P. A. Morton, and M. Lipson, "High Coupling Efficiency Etched Facet Tapers in Silicon Waveguides," *IEEE Photonics Technology Letters* **26**, 2380–2382 (2014).
 - 16 J. Notaros, F. Pavanello, M. T. Wade, C. Gentry, A. Atabaki, L. Alloatti, R. J. Ram, and M. Popovic, "Ultra-Efficient CMOS Fiber-to-Chip Grating Couplers," p. M2I.5 (2016).
 - 17 M. Davanço, M. T. Rakher, W. Wegscheider, D. Schuh, A. Badolato, and K. Srinivasan, "Efficient quantum dot single photon extraction into an optical fiber using a nanophotonic directional coupler," *Applied Physics Letters* **99**, 121101 (2011).
 - 18 S. Ates, I. Agha, A. Gulinatti, I. Rech, A. Badolato, and K. Srinivasan, "Improving the performance of bright quantum dot single photon sources using temporal filtering via amplitude modulation," *Scientific Reports* **3** (2013).
 - 19 J. W. Silverstone, R. Santagati, D. Bonneau, M. J. Strain, M. Sorel, J. L. O'Brien, and M. G. Thompson, "Qubit entanglement between ring-resonator photon-pair sources on a silicon chip," *Nature Communications* **6**, 7948 (2015).
 - 20 N. Prtljaga, R. J. Coles, J. O'Hara, B. Royall, E. Clarke, A. M. Fox, and M. S. Skolnick, "Monolithic integration of a quantum emitter with a compact on-chip beam-splitter," *Applied Physics Letters* **104**, 231107 (2014).
 - 21 K. D. Jöns, U. Rengstl, M. Oster, F. Hargart, M. Heldmaier, S. Bounouar, S. M. Ulrich, M. Jetter, and P. Michler, "Monolithic on-chip integration of semiconductor waveguides, beam splitters and single-photon sources," *Journal of Physics D: Applied Physics* **48**, 085101 (2015).
 - 22 G. Reithmaier, M. Kaniber, F. Flassig, S. Lichtmannecker, K. Mller, A. Andrejew, J. Vukovi, R. Gross, and J. J. Finley, "On-Chip Generation, Routing, and Detection of Resonance Fluorescence," *Nano Lett.* **15**, 5208–5213 (2015).
 - 23 C. P. Dietrich, A. Fiore, M. G. Thompson, M. Kamp, and S. Höfling, "GaAs integrated quantum photonics: Towards compact and multi-functional quantum photonic integrated circuits," *Laser & Photonics Reviews* pp. n/a–n/a (2016).
 - 24 A. L. Migdall, D. Branning, and S. Castelletto, "Tailoring single-photon and multiphoton probabilities of a single-photon on-demand source," *Physical Review A* **66**, 053805 (2002).

- ²⁵ M. Collins, C. Xiong, I. Rey, T. Vo, J. He, S. Shahnia, C. Rardon, T. Krauss, M. Steel, A. Clark, and B. Eggleton, “Integrated spatial multiplexing of heralded single-photon sources,” *Nature Communications* **4** (2013).
- ²⁶ R. J. Warburton, “Single spins in self-assembled quantum dots,” *Nature Materials* **12**, 483–493 (2013).
- ²⁷ K. Srinivasan and O. Painter, “Linear and nonlinear optical spectroscopy of a strongly coupled microdisk-quantum dot system,” *Nature (London)* **450**, 862–865 (2007).
- ²⁸ C. Xiong, X. Zhang, A. Mahendra, J. He, D.-Y. Choi, C. J. Chae, D. Marpaung, A. Leinse, R. G. Heideman, M. Hoekman, C. G. H. Roeloffzen, R. M. Oldenbeuving, P. W. L. van Dijk, C. Taddei, P. H. W. Leong, and B. J. Eggleton, “Compact and reconfigurable silicon nitride time-bin entanglement circuit,” *Optica* **2**, 724 (2015).
- ²⁹ T. P. Purdy, K. E. Grutter, K. Srinivasan, and J. M. Taylor, “Observation of Optomechanical Quantum Correlations at Room Temperature,” arXiv:1605.05664 [cond-mat, physics:physics, physics:quant-ph] (2016), arXiv: 1605.05664.
- ³⁰ J. E. Bowers, T. Komljenovic, M. Davenport, J. Hulme, A. Y. Liu, C. T. Santis, A. Spott, S. Srinivasan, E. J. Stanton, and C. Zhang, “Recent advances in silicon photonic integrated circuits,” p. 977402 (2016).
- ³¹ I. J. Luxmoore, R. Toro, O. D. Pozo-Zamudio, N. A. Wasley, E. A. Chekhovich, A. M. Sanchez, R. Beanland, A. M. Fox, M. S. Skolnick, H. Y. Liu, and A. I. Tartakovskii, “III–V quantum light source and cavity-QED on Silicon,” *Scientific Reports* **3** (2013).
- ³² Y. Chen, J. Zhang, M. Zopf, K. Jung, Y. Zhang, R. Keil, F. Ding, and O. G. Schmidt, “Wavelength-tunable entangled photons from silicon-integrated IIIV quantum dots,” *Nature Communications* **7**, 10 387 (2016).
- ³³ I. E. Zadeh, A. W. Elshaari, K. D. Jns, A. Fognini, D. Dalacu, P. J. Poole, M. E. Reimer, and V. Zwiller, “Deterministic Integration of Single Photon Sources in Silicon Based Photonic Circuits,” *Nano Lett.* **16**, 2289–2294 (2016).
- ³⁴ S. L. Mouradian, T. Schrder, C. B. Poitras, L. Li, J. Goldstein, E. H. Chen, M. Walsh, J. Cardenas, M. L. Markham, D. J. Twitchen, M. Lipson, and D. Englund, “Scalable Integration of Long-Lived Quantum Memories into a Photonic Circuit,” *Phys. Rev. X* **5**, 031 009 (2015).
- ³⁵ E. Murray, D. J. P. Ellis, T. Meany, F. F. Floether, J. P. Lee, J. P. Griffiths, G. A. C. Jones, I. Farrer, D. A. Ritchie, A. J. Bennett, and A. J. Shields, “Quantum photonics hybrid integration platform,” *Applied Physics Letters* **107**, 171 108 (2015).
- ³⁶ S. Khasminskaya, F. Pyatkov, K. Sowik, S. Ferrari, O. Kahl, V. Kovalyuk, P. Rath, A. Vetter, F. Hennrich, M. M. Kappes, G. Gol’tsman, A. Korneev, C. Rockstuhl, R. Krupke, and W. H. P. Pernice, “Fully integrated quantum photonic circuit with an electrically driven light source,” *Nature Photonics* **advance online publication** (2016).
- ³⁷ R. J. Coles, D. M. Price, J. E. Dixon, B. Royall, E. Clarke, P. Kok, M. S. Skolnick, A. M. Fox, and M. N. Makhonin, “Chirality of nanophotonic waveguide with embedded quantum emitter for unidirectional spin transfer,” *Nature Communications* **7**, 11 183 (2016).
- ³⁸ J. Bleuse, J. Claudon, M. Creasey, N. S. Malik, J.-M. Gérard, I. Maksymov, J.-P. Hugonin, and P. Lalanne, “Inhibition, Enhancement, and Control of Spontaneous Emission in Photonic Nanowires,” *Phys. Rev. Lett.* **106**, 103 601 (2011).
- ³⁹ J. Claudon, J. Bleuse, N. S. Malik, M. Bazin, P. Jaffrenou, N. Gregersen, C. Sauvan, P. Lalanne, and J. Gérard, “A highly efficient single-photon source based on a quantum dot in a photonic nanowire,” *Nature Photonics* **4**, 174–177 (2010).
- ⁴⁰ M. Davanço and K. Srinivasan, “Fiber-coupled semiconductor waveguides as an efficient optical interface to a single quantum dipole,” *Opt. Lett.* **34**, 2542–2544 (2009).
- ⁴¹ V. S. C. Manga Rao and S. Hughes, “Single quantum-dot Purcell factor and β factor in a photonic crystal waveguide,” *Physical Review B* **75**, 205 437 (2007).
- ⁴² T. Lund-Hansen, S. Stobbe, B. Julsgaard, H. Thyrrstrup, T. Süner, M. Kamp, A. Forchel, and P. Lodahl, “Experimental Realization of Highly Efficient Broadband Coupling of Single Quantum Dots to a Photonic Crystal Waveguide,” *Physical Review Letters* **101**, 113 903 (2008).
- ⁴³ F. Xia, V. M. Menon, and S. R. Forrest, “Photonic integration using asymmetric twin-waveguide (ATG) technology: part I—concepts and theory,” *IEEE Journal of Selected Topics in Quantum Electronics* **11**, 17–29 (2005).
- ⁴⁴ A. Stintz, G. T. Liu, H. Li, L. F. Lester, and K. J. Malloy, “Low-threshold current density 1.3- μ m InAs quantum-dot lasers with the dots-in-a-well (DWELL) structure,” *IEEE Photonics Technology Letters* **12**, 591–593 (2000).
- ⁴⁵ L. Sapienza, M. Davanço, A. Badolato, and K. Srinivasan, “Nanoscale optical positioning of single quantum dots for bright and pure single-photon emission,” *Nature Communications* **6**, 7833 (2015).
- ⁴⁶ A. Dousse, L. Lanco, J. Suffczyński, E. Semenova, A. Mirard, A. Lemaître, I. Sagnes, C. Roblin, J. Bloch, and P. Senellart, “Controlled Light-Matter Coupling for a Single Quantum Dot Embedded in a Pillar Microcavity Using Far-Field Optical Lithography,” *Physical Review Letters* **101**, 267 404 (2008).
- ⁴⁷ C. Santori, D. Fattal, J. Vučković, G. S. Solomon, E. Waks, and Y. Yamamoto, “Submicrosecond correlations in photoluminescence from InAs quantum dots,” *Physical Review B* **69**, 205 324 (2004).
- ⁴⁸ M. Davanço, C. S. Hellberg, S. Ates, A. Badolato, and K. Srinivasan, “Multiple time scale blinking in InAs quantum dot single-photon sources,” *Physical Review B* **89**, 161 303 (2014).
- ⁴⁹ K. Srinivasan and O. Painter, “Optical fiber taper coupling and high-resolution wavelength tuning of microdisk resonators at cryogenic temperatures,” *Applied Physics Letters* **90**, 031 114 (2007).
- ⁵⁰ W. Pernice, C. Schuck, O. Minaeva, M. Li, G. Goltsman, A. Sergienko, and H. Tang, “High-speed and high-efficiency travelling wave single-photon detectors embedded in nanophotonic circuits,” *Nature Communications* **3**, 1325 (2012).
- ⁵¹ R. Verberk and M. Orrit, “Photon statistics in the fluorescence of single molecules and nanocrystals: Correlation functions versus distributions of on- and off-times,” *The Journal of Chemical Physics* **119**, 2214–2222 (2003).
- ⁵² M. Köllner and J. Wolfrum, “How many photons are necessary for fluorescence-lifetime measurements?” *Chemical Physics Letters* **200**, 199–204 (1992).

SUPPLEMENTARY INFORMATION

I. EXTENDED DISCUSSION: QUANTUM PHOTONIC INTEGRATED CIRCUITS WITH QUANTUM DOTS

The considerable potential of InAs/GaAs quantum dots (QDs), both for triggered single-photon generation and as quantum logic elements, has spurred the development of a number of platforms that seek to incorporate these QDs within photonic circuits. A direct method is to develop both active and passive components within the same material system. Along these lines, monolithic GaAs-based quantum photonic circuits with on-chip quantum dot-based single-photon sources have been demonstrated by a number of research groups¹. Two general approaches have been adopted. In the first, passive circuits are composed of low-index-contrast GaAs/AlGaAs ridge waveguides produced on top of a GaAs/AlGaAs substrate^{2,3}. Such waveguide geometries can be produced with relatively straightforward fabrication processes, relying solely on epitaxial growth for vertical optical confinement and a single etching step for lateral confinement. Due to the small vertical refractive index contrast that is achievable through growth, waveguide cross-section dimensions are typically of the order of microns. While lower refractive indices are generally desirable for minimizing scattering losses in propagation, large mode field diameters (and large mode volumes in the case of cavities) translate into less compact devices, less effective light-matter interactions, and less effective geometrical control of waveguide dispersion (relevant for on-chip nonlinear optics). In particular, weak vertical confinement means more effective dipolar coupling to substrate radiative modes, translating into a reduced β -factor for radiating dipoles (see main text). Distributed-feedback reflector-based geometries such as in ref. 2 can ameliorate this, however the achievable mode-field diameters are also limited by the relatively small index contrast between GaAs and AlGaAs. All of these issues are to great extent circumvented in the second approach, in which circuits composed of suspended GaAs waveguides surrounded by air or vacuum, either of the channel⁴ or photonic crystal⁵ types (or both), are implemented. In this case, the strong index contrast allows strong transverse field confinement in waveguides of cross-sectional dimensions of the order of hundreds of nanometers. Small modal areas and cavity mode volumes can be achieved, meaning stronger light-matter interactions and higher β -factors for radiating dipoles⁶, together with strong geometry-based control of waveguide dispersion. An important limitation of such an approach, however, is the losses due to scattering at the etched sidewalls, which can be considerably higher due to the strong index contrast between the semiconductor and the air. A second issue is that the fragility of suspended GaAs structures imposes limits on the dimensions of free-standing circuits, requiring support structures such as tethers or transitions to non-suspended waveguides, which may induce significant scattering losses⁵. Fabrication, device handling, and further integration with other types of on-chip elements are also more cumbersome in this case. An additional challenge common to both approaches is that passive circuits are produced in the same material layer that contains the QDs. Because there is no strict separation between active and passive portions of the photonic circuit, the population of QDs inside the passive section can contribute to excess optical absorption.

As discussed in the main text, our heterogeneous integration platform offers essentially all the advantages of the two approaches described above, while addressing many of the aforementioned challenges. The large refractive index contrast between GaAs and Si_3N_4 allows for strong modal confinement within the GaAs layer so that large β factors can be achieved in the active quantum dot region. This large refractive index contrast is, in addition, achieved without requiring devices to be undercut, improving the mechanical and thermal stability of the system, particularly as the number of integrated elements increases. Furthermore, complete removal of the GaAs material outside in the passive regions avoids excess optical absorption due to the background QD ensemble. Within the passive sections, the large refractive index contrast between Si_3N_4 and SiO_2 enables the dispersion engineering and large effective nonlinearity needed for nonlinear optics applications, such as frequency downconversion of the QD emission to the 1550 nm telecom band⁷. Such nonlinear optics applications can in principle be implemented in suspended GaAs photonic circuits, though the much wider bandgap of Si_3N_4 and SiO_2 in comparison to GaAs-based materials ensures that two-photon absorption, an important factor in nonlinear nanophotonic devices, is negligible over a wide range of wavelengths. Coupling off-chip to optical fibers can also be optimized, as our platform is compatible with end-fire approaches that utilize inverse tapers and symmetric low-index claddings^{8,9}. In particular, devices can be designed to admit a full SiO_2 cladding rather than the current top air cladding, with additional processing likely consisting of a single additional PECVD deposition step.

While all of the fabrication steps that we have demonstrated in this work are scalable, the random nature of the in-plane spatial locations of self-assembled InAs/GaAs QDs is a limitation on the overall yield and ability to, for example, integrate multiple QD sites together within a passive Si_3N_4 circuit. Going forward, we note that developments in site-controlled QD growth¹⁰⁻¹² will help to address this issue, and in general will be compatible with our fabrication approach. In the near-term, we can envision pre-characterization of QDs after creating the bonded wafer stack, such that GaAs devices are only created in regions for which desirable single QD behavior has been confirmed. In particular, photoluminescence imaging¹³ has been confirmed as a technique for locating the position of single InAs/GaAs QDs with respect to alignment features, and recent implementations¹⁴ have demonstrated the location of single QDs within $\approx 5000 \mu\text{m}^2$ spatial regions with sub-10 nm positioning uncertainty, with typical image acquisition times of 1 s. We anticipate that such an approach can enable a higher throughput than pick-and-place techniques¹⁵⁻¹⁸, which also require pre-screening of the quantum emitters along with the additional assembly steps.

II. FABRICATION DETAILS

To produce the starting wafer stack shown in Fig. 3a of the main text, we utilized the low-temperature plasma-activated direct wafer bonding procedure of ref. 19. The layer stack for the two wafers that are bonded in this procedure, one silicon-based and one GaAs-based, are given in tables I and II respectively. The Si_3N_4 layer of the silicon-based stack in table I was grown with low-pressure chemical vapor deposition, and the epilayer stack of table II was grown via molecular beam epitaxy.

TABLE I: Si_3N_4 wafer stack

Layer	Material	Thickness (nm)
Waveguide	Si_3N_4	550
Bottom cladding	Thermal SiO_2	3000
Substrate	Si	-

TABLE II: GaAs Epilayer Stack

Layer	Material	Thickness (nm)
Surface cap	GaAs	10
Waveguide top	$\text{Al}_{0.30}\text{Ga}_{0.70}\text{As}$	40
Waveguide top	GaAs	74
Quantum well	$\text{In}_{0.15}\text{Ga}_{0.85}\text{As}$	6
Quantum dot	InAs	2.4 monolayer
Barrier	$\text{In}_{0.15}\text{Ga}_{0.85}\text{As}$	1
Waveguide bottom	GaAs	74
Sacrificial layer	$\text{Al}_{0.30}\text{Ga}_{0.70}\text{As}$	50
Sacrificial layer	$\text{Al}_{0.70}\text{Ga}_{0.30}\text{As}$	1500
Substrate	GaAs	-

A ≈ 30 nm layer of SiN was deposited on top of cleaved (≈ 5 mm²) pieces of the III-V epiwafer with plasma-enhanced chemical vapor deposition (PECVD). Contact lithography followed by reactive ion etching in a $\text{CHF}_3/\text{O}_2/\text{Ar}$ plasma was used to produce $\approx 10\mu\text{m}$ wide, ≈ 1 cm long, ≈ 30 nm deep channels on the Si_3N_4 wafer surface, prior to bonding. This was done to prevent the formation of trapped H_2 bubbles at the bonding interface during the annealing process¹⁹. The Si_3N_4 wafer was then cleaved into small (≈ 2 cm²) pieces.

For wafer bonding, the surfaces of the GaAs and Si_3N_4 wafer pieces were cleaned in acetone, then activated in an O_2 plasma for 1 minute, at a pressure of 26.7 Pa (200 mTorr), flow of 1.5×10^{-5} O_2 mol/s (20 sccm) and 200 W radio-frequency power. Pairs of wafers were then placed in contact and pre-bonded under light manual contact. The pre-bonded samples were next annealed at 300 °C for 1 hour in a nitrogen-purged environment to produce a permanent bond. The warm-up and cool-down rates were set to 5 °C/min. At this point, samples consisted of small, rectangular-shaped GaAs wafer pieces permanently bonded onto the surface of larger Si_3N_4 wafers.

We next carefully covered the exposed Si_3N_4 areas on the wafers with Apiezon W wax²⁰ that had been previously dissolved in trichloroethylene (TCE). The dissolved wax wetted the Si_3N_4 surfaces and the sidewalls of the bonded GaAs pieces, however not the exposed back surfaces of the GaAs wafer. We placed the samples on a hotplate at 80 °C for 30 minutes to evaporate the TCE, solidifying the wax. The samples were next immersed in a 3:7 $\text{H}_3\text{PO}_4:\text{H}_2\text{O}_2$ solution for approximately 5 hours, to remove most of the GaAs substrate. They were then transferred to a 4:1 citric acid (50 % mass fraction): H_2O_2 solution, which etched GaAs with a very high selectivity with respect to the AlGaAs sacrificial layers. The samples were left in for approximately 5 hours, until the exposed GaAs wafer surface looked uniform and unchanged. At this point, the GaAs substrate had been completely removed. Next, the samples were dipped in 49 % HF for 30 seconds to remove the AlGaAs sacrificial layers. Finally, the wax was removed with TCE.

Following the wafer bonding step, fabrication proceeded as described in the main text. Further details are provided here. An array of Au alignment marks was first produced on top of the GaAs layer via electron-beam lithography followed by metal-lift-off. A bilayer polymethylmethacrylate/copolymer resist process was used. An electron-beam evaporator was used to deposit a 10 nm Cr adhesion layer, and a 50 nm Au layer. Lift-off was carried out in an acetone bath. Electron-beam lithography with ZEP 520A²⁰ resist followed by inductively-coupled plasma etching using a $\text{Cl}_2:\text{Ar}$ chemistry were next used to define GaAs devices aligned to the Au mark array. Because ZEP520A is a positive-tone resist, devices were defined by etching the GaAs only in micron-size areas that surrounded the devices. To remove the remaining GaAs from the rest of the wafer surface, we used a wet-etch approach. First, e-beam lithography with ma-N 2045negative tone resist²⁰ was performed to define protection patterns that covered only the device areas and a selected number of Au alignment marks (a protection patch is highlighted in the optical micrograph Fig. 3b in the main text, covering the GaAs microring resonator and bus waveguide). The samples were then immersed in TFA gold etchant for ≈ 1 min, then in 1020 Cr etch solution for ≈ 1 min. This removed exposed Cr/Au alignment marks, as well as the exposed GaAs layer. The wet etch procedure could be repeated several times without affecting the resist protection layer. Acetone was afterwards used to remove the ma-N resist.

After cleanup of the etched sample surface, a second electron-beam lithography exposure was performed, referenced to the original Au mark array, to define Si_3N_4 waveguide patterns aligned to the previously etched GaAs devices. We emphasize that the alignment marks used were from the original mark array, and were protected during the GaAs wet etch step. Reactive ion etching (RIE) in a CHF_3/CF_4 plasma was

used to produce the Si_3N_4 waveguides. The chip was finally cleaved perpendicular to the Si_3N_4 waveguides > 1 mm away from the GaAs devices, to allow access with optical fibers in the endfire configuration.

III. ROOM TEMPERATURE PHOTONIC CHARACTERIZATION SETUP

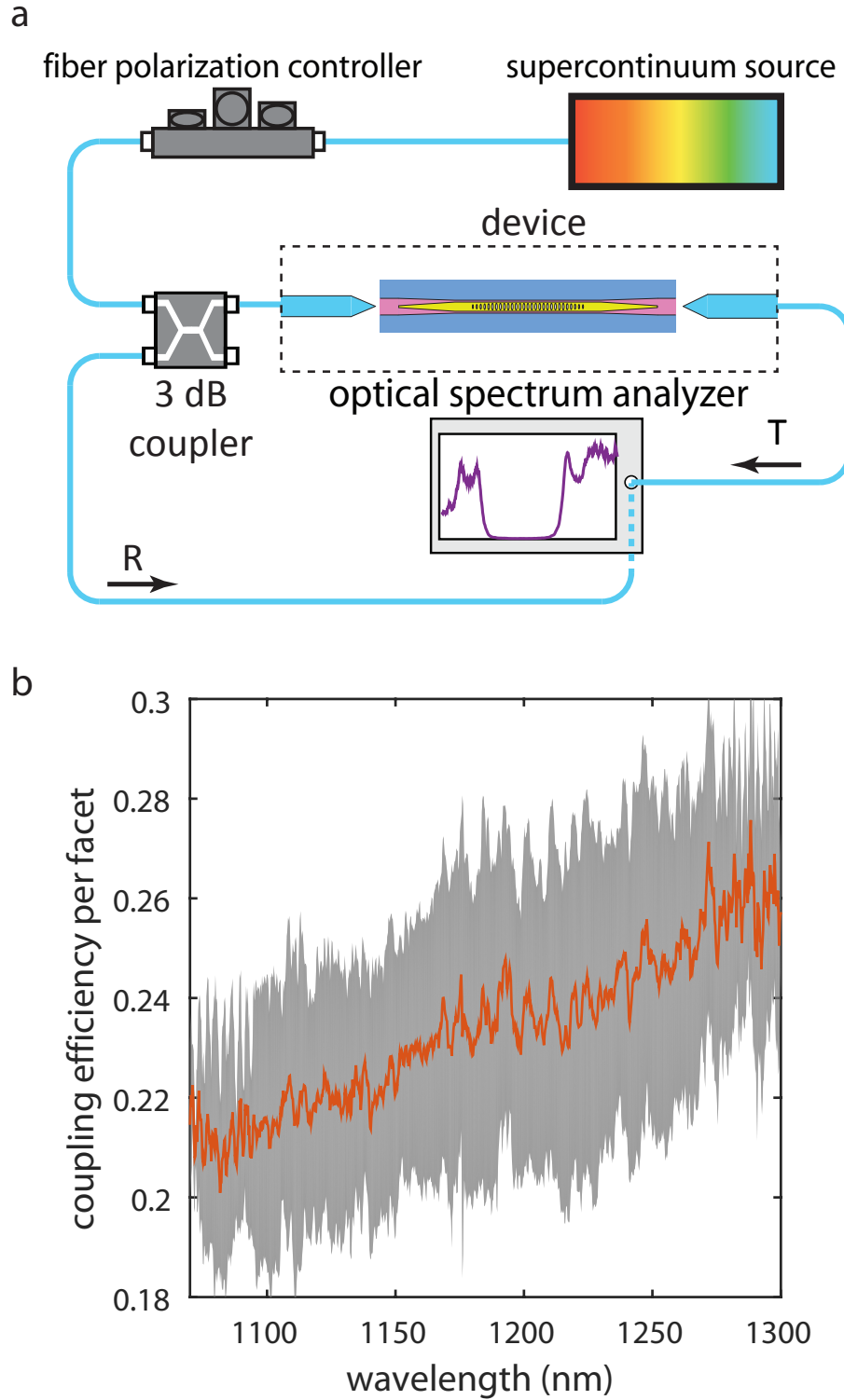


FIG. S1: **Photonic characterization setup.** **a**, Experimental setup for passive, endfire coupling measurement of transmitted (T) and reflected (R) power. **b**, Measured coupling efficiency per facet (including fiber-to-waveguide coupling and propagation losses in the waveguide between the facet and a GaAs device) as a function of wavelength. The red curve and grey area are the mean value and standard deviation over three measured waveguides.

IV. CRYOGENIC MEASUREMENT EXPERIMENTAL SETUP

The setup used for low temperature cryogenic measurements is shown in Fig. S2. Samples were placed on a fixed mount inside a liquid Helium flow cryostat and cooled down ≈ 7 K. A microscope consisting of a long-working distance objective (20 \times , NA=0.4), beamsplitter (BS) and combination zoom lens / illuminator system mounted at the top cryostat window allowed devices on the sample surface to be imaged. An example image of a GaAs microring resonator device can be seen in the "sample imaging" box in the schematic of Fig. S2. Light from an external cavity tunable laser (ECDL) with center wavelength around 1060 nm was introduced into the objective via the beamsplitter, to produce a small ($\approx 5 \mu\text{m}$) spot that pumped QDs at select locations on the device under test. As discussed in the main text, photoluminescence from the QDs was coupled to Si_3N_4 waveguides, and collected at the cleaved edge of the chip with a lensed fiber. A nanopositioning stage stack placed inside the cryostat allowed the lensed fibers to be aligned to waveguide facets, as illustrated in Fig. S2.

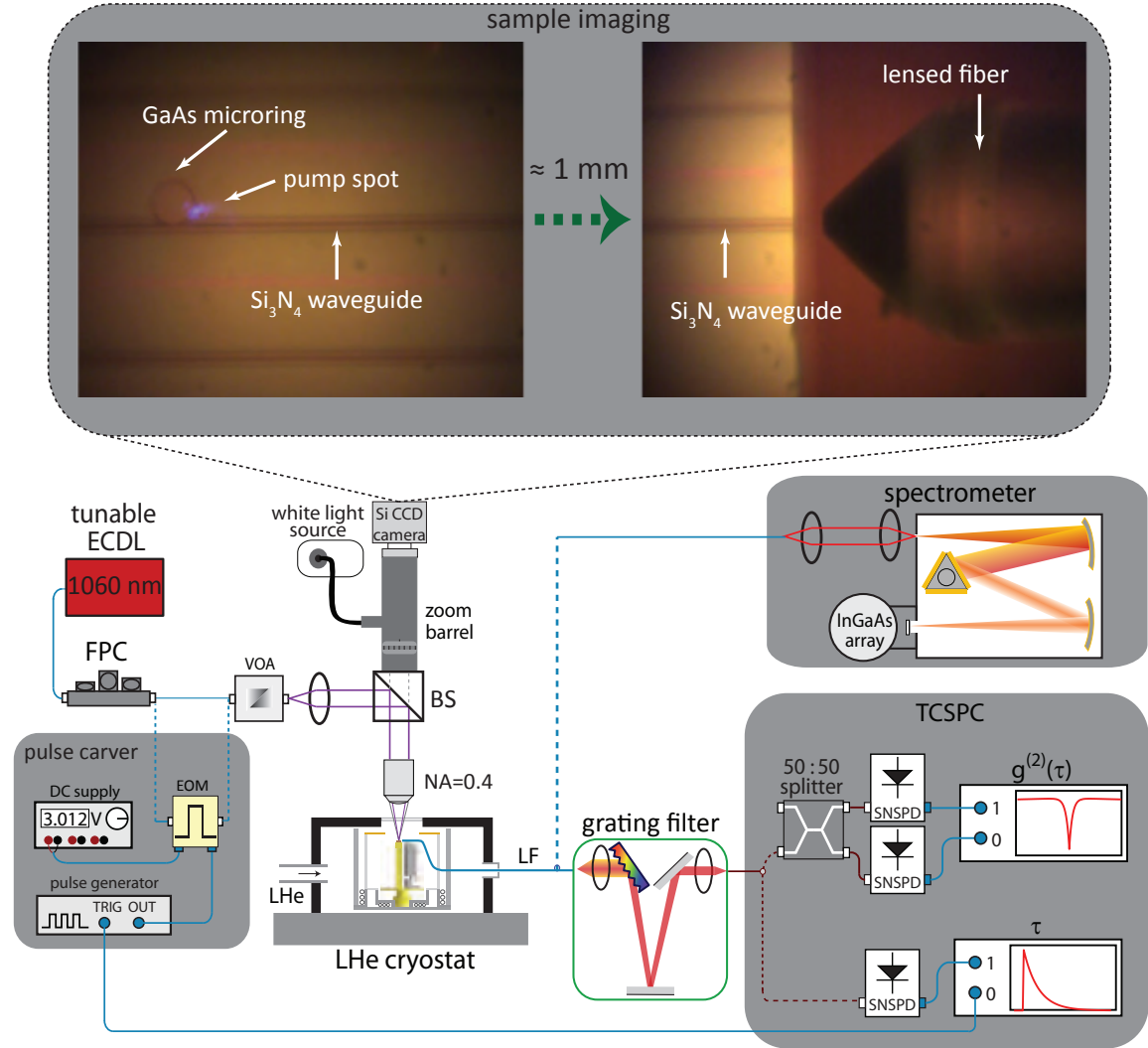


FIG. S2: **Cryogenic measurement setup.** Devices are tested inside a liquid Helium flow cryostat. A window at the top allows imaging of the sample, as shown in the "sample imaging" box. Devices are also pumped from the top with laser light (purple spot over portion of the GaAs microring resonator), and quantum dot photoluminescence is coupled into the Si_3N_4 waveguide. The emitted light travels ≈ 1 mm down the Si_3N_4 waveguide until the cleaved edge of the chip, where it is collected with a lensed fiber mounted to a nanopositioning stage inside the cryostat. The collected light can then be routed to a grating spectrometer, or filtered in a grating filter and then routed towards time-correlated single-photon counting measurements. Pulsed pumping can be achieved by modulating continuous-wave laser light with an electro-optic modulator. ECDL: external-cavity diode laser; FPC: fiber polarization controller; EOM: electro-optic modulator; BS: beamsplitter; VOA: variable optical attenuator. LF: lensed fiber. SNSPD: superconducting nanowire single-photon detector; TCSPC: time-correlated single-photon counting; CCD: charge-coupled device; LHe: liquid Helium

The collected photoluminescence was either be routed to a grating spectrometer equipped with a liquid-nitrogen cooled InGaAs photodiode array, or filtered through a ≈ 700 pm bandpass tunable grating filter and then routed towards our single-photon detection system for time-correlated single-photon counting (TCSPC) measurements of excited state lifetime and second-order correlations. For correlation measurements, we used a Hanbury-Brown and Twiss setup consisting of fiber-based 50:50 beamsplitter connected to two amorphous WSi superconducting nanowire single-photon detectors (SNSPDs)²¹. Detector counts were correlated in a TCSPC unit.

For lifetime measurements, a 10 GHz lithium niobate electro-optic modulator (EOM) was used to produce a 80 MHz, ≈ 200 ps pulse train from the CW ECDL laser²². A fiber-based polarization controller (FPC) was used to control the polarization of the ECDL light going into the EOM, and a DC bias was applied to the EOM to maximize signal extinction. An electrical pulsed source was used to produce an 80 MHz train of ≈ 200 ps pulses of < 1 V peak amplitude, which was then amplified and used to drive the EOM modular via its radio frequency (RF) port. A trigger signal from the pulse generator served as the reference channel in our TCSPC system. Figure S3a shows a typical temporal profile for the pulses produced by the EOM, detected with an SNSPD. Pulse FWHM of ≈ 200 ps and > 20 dB extinction are observed. The pulsed electrical signal produced small satellite peaks that were imprinted in the optical signal, as indicated in Fig. S3a. Impulse response functions (IRFs) such as shown in Fig. S3a were used in decay lifetime fits as explained below, so that the effect of satellite peaks, though minimal, was accounted for.

To determine the time resolution of our detection system, we launched attenuated, few-picosecond pulses from a Ti:Sapphire mode-locked laser at 975 nm into the SNSPDs, to obtain the temporal trace in Fig. S3. The peak can be well fitted with a Gaussian with standard deviation $\sigma = 129$ ps \pm 0.04 ps (uncertainty is a 95 % least-squares fit confidence interval, corresponding to two standard deviations).

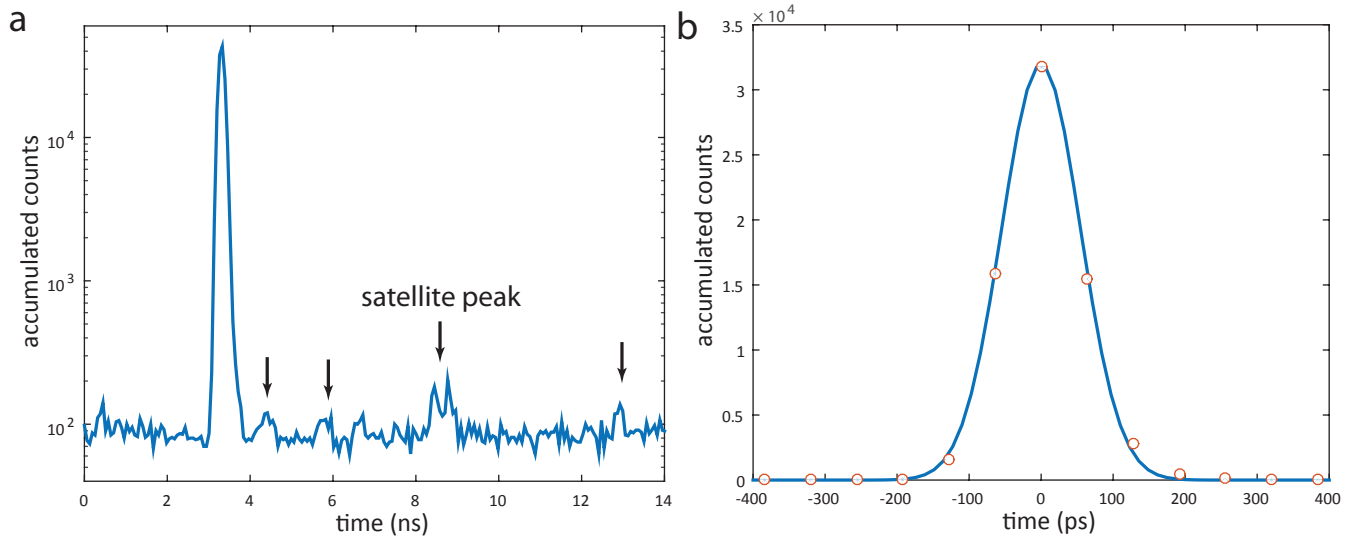


FIG. S3: **Impulse response functions.** **a**, Temporal profile of pulsed pump achieved with an electro-optic modulator (EOM). Satellite peaks due to an imperfect electrical driving signal are pinpointed with arrows. **b**, Impulse response of the SNSPD-based detection system, obtained with a \approx ps pulsed Ti:Sapphire laser source.

V. PURCELL ENHANCEMENT IN THE HETEROGENEOUS PLATFORM

Here we provide further information about the Purcell enhancement data and fits for the quantum dot in a microring resonator presented in Figs. 6d-6g of the main text. Figures S4a and S4b respectively show lifetimes and corresponding decay component amplitudes for the fits, as a function of the detuning Δ . It is apparent that the fast lifetimes vary considerably, from ≈ 414 ps at $\Delta \approx -0.26$ nm to ≈ 263 ps at $\Delta \approx -0.07$ nm, then to ≈ 1.1 ns at $\Delta = 0.84$ nm. Slow lifetimes remain consistently above 1 ns. The fast decay contribution remains above 50 % for all detunings except $\Delta \approx 0.36$ nm, where a second exciton (X_2) is seen to couple to the same whispering-gallery mode in Fig. 6f. The contributions of the two excitons and the cavity to the detected signal in the lifetime measurements is estimated through fits to the emission spectra at each detuning, shown in Fig. S4c. The X_1 contribution is seen to be dominant everywhere (except $\Delta \approx 0.36$ nm). The X_2 contribution is maximized at $\Delta \approx 0.36$ nm, but remains below 0.015 everywhere. These results indicate that the fast lifetimes can be assigned to the X_1 exciton. Further supporting this assignment is the fact that the good quality of the $g^{(2)}(\tau)$ fit in Fig. 6e was achieved by including a Poissonian background equal to the cavity contribution in the PL spectrum fit of Fig. 6d.

Uncertainties for $g^{(2)}(0)$, Δ and the X_1 , X_2 and cavity PL contributions are 95 % fit confidence intervals (two standard deviations). Uncertainties for τ are single standard deviations from the exponential decay fit procedure.

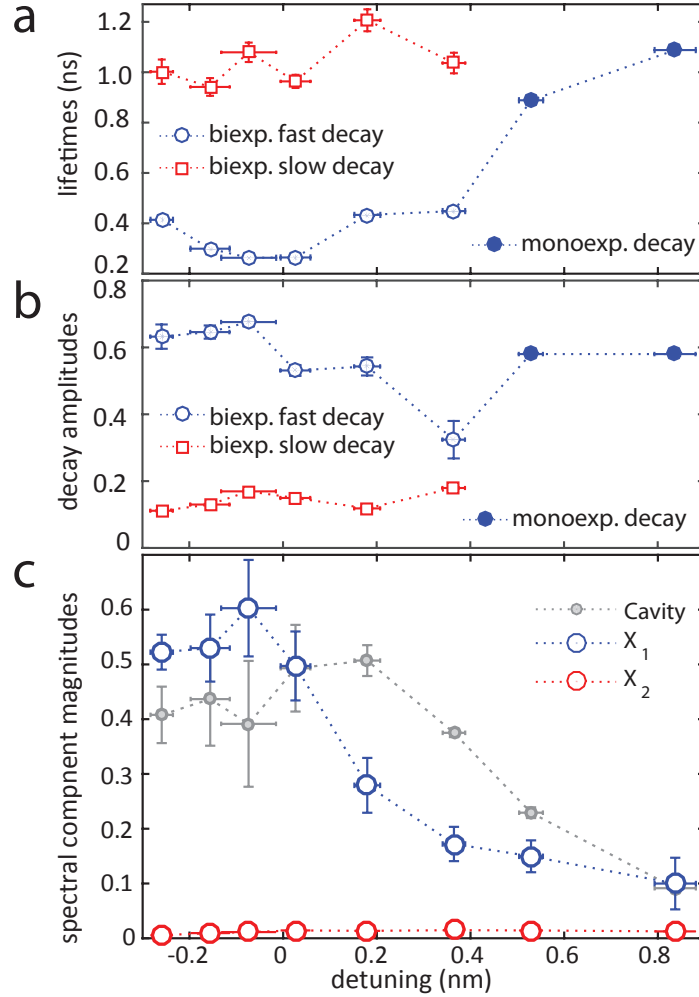


FIG. S4: **Lifetime and PL intensity fit results.** **a**, Decay lifetimes for the fits in Fig. 6f, as a function of the detuning Δ . Open blue circles and red squares are the fast and slow biexponential decay lifetimes, closed blue circles are the monoexponential decay lifetimes. **b**, Corresponding amplitudes for the different decay components. **c**, magnitudes of the X_1 , X_2 and cavity Lorentzians used to fit the PL spectra in **f**, normalized to the sum of the integrated intensities of the three components before filtering. Uncertainties for Δ and the X_1 , X_2 and cavity PL contributions are 95 % fit confidence intervals (two standard deviations). Uncertainties for τ are single standard deviations from the exponential decay fit procedure.

VI. FISHER INFORMATION MATRIX

Variances for the estimated decay lifetime parameters in θ can be obtained from the diagonal elements of the inverse of the Fisher Information Matrix $M(\theta)$ with

$$[M(\theta)]_{mn} = \mathbb{E}_{\theta} \left[\frac{\partial \ln f_{\theta}^{(k)}(Y^k)}{\partial \theta_m} \frac{\partial \ln f_{\theta}^{(k)}(Y^k)}{\partial \theta_n} \right]. \quad (\text{S1})$$

Here, \mathbb{E}_{θ} stands for expectation value, and $f_{\theta}^{(k)}(y^k)$ is the probability mass function for the counts in each bin of the lifetime trace, which constitute a sequence of random variables with multinomial distribution²³:

$$f_{\theta}^{(k)}(y^k) = \frac{N!}{\prod_{i=1}^k y_i!} \prod_{i=1}^k p_i^{y_i}(\theta), \quad \sum_{i=1}^k y_i = N, \quad \sum_{i=1}^k p_i(\theta) = 1 \quad (\text{S2})$$

Noting that

$$\frac{\partial \ln f_{\theta}^{(k)}(y^k)}{\partial \theta_m} = \sum_{i=1}^k \frac{y_i}{p_i(\theta)} \frac{\partial p_i(\theta)}{\partial \theta_m}, \quad (\text{S3})$$

we can write

$$\sum_{i=1}^k \sum_{j=1}^k \frac{\mathbb{E}_{\theta} [Y_i Y_j]}{p_i(\theta) p_j(\theta)} \frac{\partial p_i(\theta)}{\partial \theta_m} \frac{\partial p_j(\theta)}{\partial \theta_n} \quad (\text{S4})$$

Now

$$\mathbb{E}_{\theta} [Y_i Y_j] = \begin{cases} \text{var}_{\theta} [Y_i] + (\mathbb{E}_{\theta} [Y_i])^2 = (N^2 - N) p_i^2(\theta) + N p_i(\theta) & \text{if } i = j, \\ \text{COV}_{\theta} [Y_i, Y_j] + \mathbb{E}_{\theta} [Y_i] \mathbb{E}_{\theta} [Y_j] = (N^2 - N) p_i(\theta) p_j(\theta) & \text{if } i \neq j, \end{cases} \quad (\text{S5})$$

where var_{θ} and COV_{θ} are the variance and the covariance operators with respect to θ , respectively. Substituting (S5) into (S4), it follows that

$$\begin{aligned} \mathbb{E}_{\theta} \left[\frac{\partial \ln f_{\theta}^{(k)}(Y^k)}{\partial \theta_m} \frac{\partial \ln f_{\theta}^{(k)}(Y^k)}{\partial \theta_n} \right] &= \sum_{i=1}^k \frac{(N^2 - N) p_i^2(\theta) + N p_i(\theta)}{p_i^2(\theta)} \frac{\partial p_i(\theta)}{\partial \theta_m} \frac{\partial p_i(\theta)}{\partial \theta_n} \\ &\quad + \underbrace{\sum_{i=1}^k \sum_{j=1}^k}_{i \neq j} \frac{(N^2 - N) p_i(\theta) p_j(\theta)}{p_i(\theta) p_j(\theta)} \frac{\partial p_i(\theta)}{\partial \theta_m} \frac{\partial p_j(\theta)}{\partial \theta_n} \end{aligned} \quad (\text{S6})$$

The first summation can be written as

$$\sum_{i=1}^k \frac{(N^2 - N) p_i^2(\theta) + N p_i(\theta)}{p_i^2(\theta)} \frac{\partial p_i(\theta)}{\partial \theta_m} \frac{\partial p_i(\theta)}{\partial \theta_n} = (N^2 - N) \sum_{i=1}^k \frac{\partial p_i(\theta)}{\partial \theta_m} \frac{\partial p_i(\theta)}{\partial \theta_n} + N \sum_{i=1}^k \frac{1}{p_i(\theta)} \frac{\partial p_i(\theta)}{\partial \theta_m} \frac{\partial p_i(\theta)}{\partial \theta_n}. \quad (\text{S7})$$

The second summation can be written as

$$\underbrace{\sum_{i=1}^k \sum_{j=1}^k}_{i \neq j} \frac{(N^2 - N) p_i(\theta) p_j(\theta)}{p_i(\theta) p_j(\theta)} \frac{\partial p_i(\theta)}{\partial \theta_m} \frac{\partial p_j(\theta)}{\partial \theta_n} = (N^2 - N) \underbrace{\sum_{i=1}^k \sum_{j=1}^k}_{i \neq j} \frac{\partial p_i(\theta)}{\partial \theta_m} \frac{\partial p_j(\theta)}{\partial \theta_n} \quad (\text{S8})$$

Substituting (S7) and (S8) into (S6), it follows that

$$\mathbb{E}_{\theta} \left[\frac{\partial \ln f_{\theta}^{(k)}(Y^k)}{\partial \theta_m} \frac{\partial \ln f_{\theta}^{(k)}(Y^k)}{\partial \theta_n} \right] = (N^2 - N) \sum_{i=1}^k \sum_{j=1}^k \frac{\partial p_i(\theta)}{\partial \theta_m} \frac{\partial p_j(\theta)}{\partial \theta_n} + N \sum_{i=1}^k \frac{1}{p_i(\theta)} \frac{\partial p_i(\theta)}{\partial \theta_m} \frac{\partial p_i(\theta)}{\partial \theta_n}. \quad (\text{S9})$$

Noting that

$$\sum_{i=1}^k \sum_{j=1}^k \frac{\partial p_i(\theta)}{\partial \theta_m} \frac{\partial p_j(\theta)}{\partial \theta_n} = \sum_{i=1}^k \frac{\partial p_i(\theta)}{\partial \theta_m} \sum_{j=1}^k \frac{\partial p_j(\theta)}{\partial \theta_n} = \frac{\partial (\sum_{i=1}^k p_i(\theta))}{\partial \theta_m} \frac{\partial (\sum_{j=1}^k p_j(\theta))}{\partial \theta_n} = \frac{\partial(1)}{\partial \theta_m} \frac{\partial(1)}{\partial \theta_n} = 0, \quad (\text{S10})$$

it follows that

$$\mathbb{E}_{\theta} \left[\frac{\partial \ln f_{\theta}^{(k)}(Y^k)}{\partial \theta_m} \frac{\partial \ln f_{\theta}^{(k)}(Y^k)}{\partial \theta_n} \right] = N \sum_{i=1}^k \frac{1}{p_i(\theta)} \frac{\partial p_i(\theta)}{\partial \theta_m} \frac{\partial p_i(\theta)}{\partial \theta_n}. \quad (\text{S11})$$

We next define

$$p_i(\tau) = e^{-ir/k} \frac{e^{r/k} - 1}{1 - e^{-r}}, \quad r \triangleq \frac{i \cdot \Delta t}{\tau} \quad (\text{S12})$$

$$\frac{\partial p_i(\tau)}{\partial \tau} = \frac{-r}{\tau} p_i(\tau) \left(-\frac{i}{k} + \frac{e^{r/k}}{(e^{r/k} - 1)k} - \frac{e^{-r}}{1 - e^{-r}} \right). \quad (\text{S13})$$

For a monoexponential decay when a portion b of the signal is due to background emission,

$$p_i(\tau, b) = \frac{b}{k} + (1 - b)p_i(\tau) \quad (\text{S14})$$

The Fisher matrix in this case can be computed with eq.(S11) and

$$\frac{\partial p_i(\tau, b)}{\partial b} = \frac{1}{k} - p_i(\tau) \quad (\text{S15})$$

$$\frac{\partial p_i(\tau, b)}{\partial \tau} = (1 - b) \frac{-r}{\tau} p_i(\tau) \left(-\frac{i}{k} + \frac{e^{r/k}}{(e^{r/k} - 1)k} - \frac{e^{-r}}{1 - e^{-r}} \right) \quad (\text{S16})$$

For biexponential decay with a background, let $\tau \triangleq (\tau_1, \tau_2)^T$. Then $p_i(\tau, a, b)$ (where a is the contribution of the first exponential decay) may be expressed as

$$p_i(\tau, b, a) = \frac{b}{k} + (1 - b) [ap_i(\tau_1) + (1 - a)p_i(\tau_2)] \quad (\text{S17})$$

The Fisher matrix in this case can be computed with eq.(S11) and

$$\frac{\partial p_i(\tau, b, a)}{\partial b} = \frac{1}{k} - [ap_i(\tau_1) + (1 - a)p_i(\tau_2)] \quad (\text{S18})$$

$$\frac{\partial p_i(\tau, b, a)}{\partial \tau_1} = a(1 - b) \frac{\partial p_i(\tau_1)}{\partial \tau_1} \quad (\text{S19})$$

$$\frac{\partial p_i(\tau, b, a)}{\partial \tau_2} = (1 - a)(1 - b) \frac{\partial p_i(\tau_2)}{\partial \tau_2} \quad (\text{S20})$$

$$\frac{\partial p_i(\tau, b, a)}{\partial a} = (1 - b) (p_i(\tau_1) - p_i(\tau_2)). \quad (\text{S21})$$

VII. OPTIMIZED DIPOLE COUPLING INTO THE HYBRID WAVEGUIDE

Here we present simulation results for the fundamental TE GaAs mode β -factor of two optimized emission capture structures. In both cases, the active waveguide section is as shown in Fig. S5a. The GaAs waveguide has a thickness of 190 nm, and the Si_3N_4 waveguide width is 600 nm. A 100 nm layer of SiO_2 separates the two waveguides. Such a layer can be produced with PECVD, same as the nitride layer grown on our GaAs wafer prior to bonding, without adversely affecting the bond quality. For the first optimized geometry, Fig. S5b, the Si_3N_4 thickness is 550 nm, similar to the Si_3N_4 waveguides in our sample. In Fig. S5c, the Si_3N_4 thickness is 250 nm. In both cases, $\beta > 0.46$ for modes propagating in either $+z$ or $-z$ directions ($2\beta > 0.92$ altogether), for a wavelength range of tens of nanometers around 1100 nm, for GaAs waveguide widths close to 300 nm.

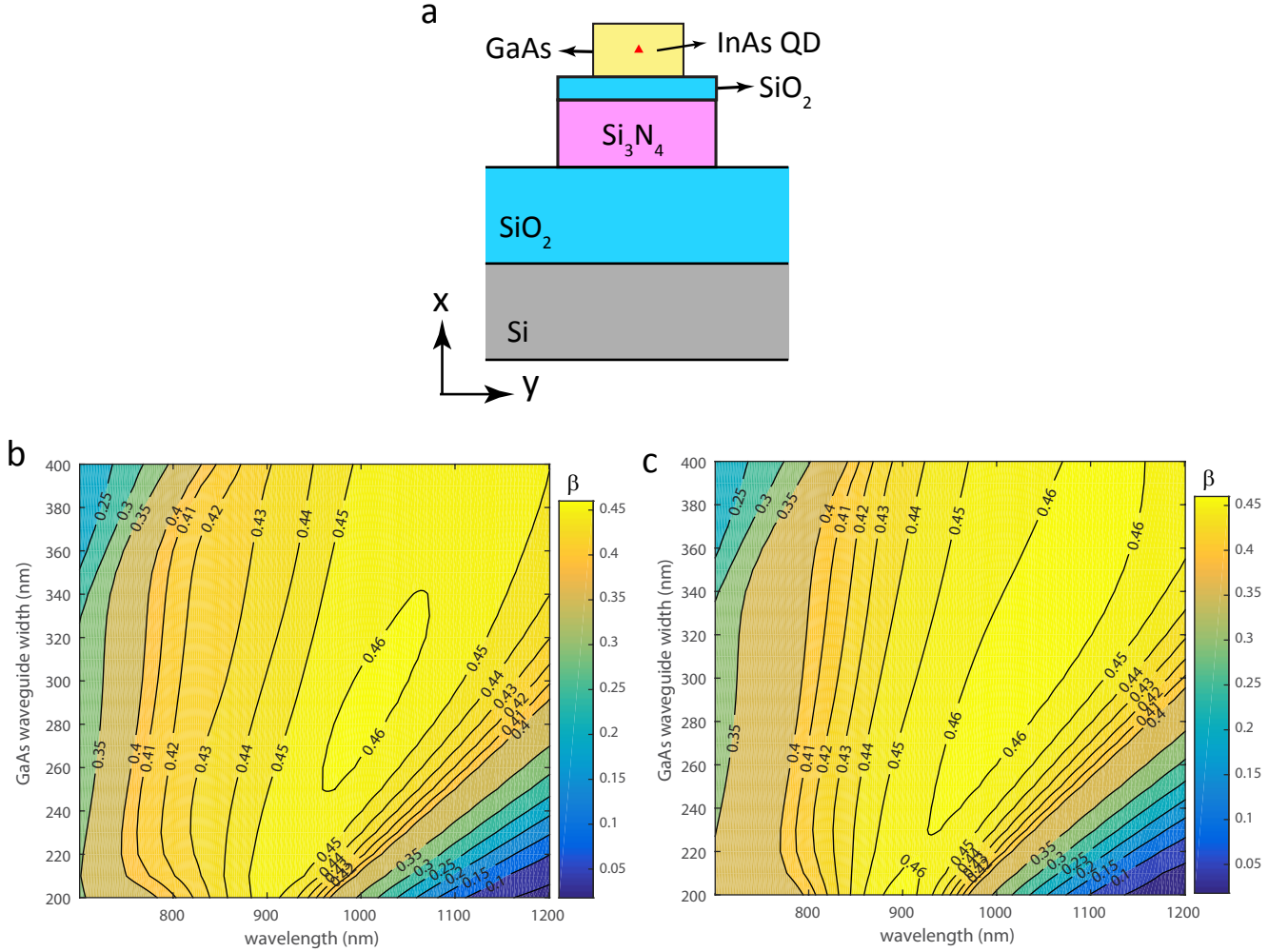


FIG. S5: β -factors in optimized structures. **a** Emission capture structure cross-section. **b** β factors as a function of wavelength and GaAs waveguide width for the fundamental TE GaAs mode, for a GaAs waveguide with thickness of 190 nm, Si_3N_4 waveguide has a width of 600 nm and thickness of 550 nm. A 100 nm thick layer of SiO_2 separates the Si_3N_4 and GaAs waveguides. The Si_3N_4 dimensions here are relevant for optical nonlinearities, as discussed in the main text. **c**, same as **a** for a 250 nm Si_3N_4 thickness, relevant for linear optics applications.

- * Electronic address: marcelo.davanco@nist.gov
- † Electronic address: liujin23@mail.sysu.edu.cn
- ‡ Electronic address: kartik.srinivasan@nist.gov
- ¹ C. P. Dietrich, A. Fiore, M. G. Thompson, M. Kamp, and S. Höfling, “GaAs integrated quantum photonics: Towards compact and multi-functional quantum photonic integrated circuits,” *Laser & Photonics Reviews* pp. n/a–n/a (2016).
 - ² K. D. Jöns, U. Rengstl, M. Oster, F. Hargart, M. Heldmaier, S. Bounouar, S. M. Ulrich, M. Jetter, and P. Michler, “Monolithic on-chip integration of semiconductor waveguides, beamsplitters and single-photon sources,” *Journal of Physics D: Applied Physics* **48**, 085 101 (2015).
 - ³ G. Reithmaier, M. Kaniber, F. Flassig, S. Lichtmannecker, K. Müller, A. Andrejew, J. Vukovi, R. Gross, and J. J. Finley, “On-Chip Generation, Routing, and Detection of Resonance Fluorescence,” *Nano Lett.* **15**, 5208–5213 (2015).
 - ⁴ N. Prtljaga, R. J. Coles, J. O’Hara, B. Royall, E. Clarke, A. M. Fox, and M. S. Skolnick, “Monolithic integration of a quantum emitter with a compact on-chip beam-splitter,” *Applied Physics Letters* **104**, 231 107 (2014).
 - ⁵ S. F. Poor, T. B. Hoang, L. Midolo, C. P. Dietrich, L. H. Li, E. H. Linfield, J. F. P. Schouwenberg, T. Xia, F. M. Pagliano, F. W. M. v. Otten, and A. Fiore, “Efficient coupling of single photons to ridge-waveguide photonic integrated circuits,” *Applied Physics Letters* **102**, 131 105 (2013).
 - ⁶ M. Davanço and K. Srinivasan, “Fiber-coupled semiconductor waveguides as an efficient optical interface to a single quantum dipole,” *Opt. Lett.* **34**, 2542–2544 (2009).
 - ⁷ Q. Li, M. Davanço, and K. Srinivasan, “Efficient and low-noise single-photon-level frequency conversion interfaces using silicon nanophotonics,” *Nat Photon* **10**, 406–414 (2016).
 - ⁸ T. Shoji, T. Tsuchizawa, T. Watanabe, K. Yamada, and H. Morita, “Low loss mode size converter from 0.3 μm square Si wire waveguides to singlemode fibres,” *Electronics Letters* **38**, 1669–1670 (2002).
 - ⁹ T. Tsuchizawa, K. Yamada, H. Fukuda, T. Watanabe, J.-i. Takahashi, M. Takahashi, T. Shoji, E. Tamechika, S. Itabashi, and H. Morita, “Microphotonics devices based on silicon microfabrication technology,” *IEEE Journal of Selected Topics in Quantum Electronics* **11**, 232–240 (2005).
 - ¹⁰ B. Rigal, C. Jarlov, P. Gallo, B. Dwir, A. Rudra, M. Calic, and E. Kapon, “Site-controlled quantum dots coupled to a photonic crystal molecule,” *Applied Physics Letters* **107**, 141 103 (2015).
 - ¹¹ C. Schneider, A. Huggenberger, M. Gschrey, P. Gold, S. Rodt, A. Forchel, S. Reitzenstein, S. Höfling, and M. Kamp, “In(Ga)As/GaAs site-controlled quantum dots with tailored morphology and high optical quality,” *physica status solidi (a)* **209**, 2379–2386 (2012).
 - ¹² M. Helfrich, P. Schroth, D. Grigoriev, S. Lazarev, R. Felici, T. Slobodskyy, T. Baumbach, and D. M. Schaadt, “Growth and characterization of site-selective quantum dots,” *physica status solidi (a)* **209**, 2387–2401 (2012).
 - ¹³ L. Sapienza, M. Davanço, A. Badolato, and K. Srinivasan, “Nanoscale optical positioning of single quantum dots for bright and pure single-photon emission,” *Nature Communications* **6**, 7833 (2015).
 - ¹⁴ J. Liu, M. Davanco, and K. Srinivasan, “Cryogenic photoluminescence imaging system for nanoscale positioning of single quantum emitters,” (2016), manuscript in preparation.
 - ¹⁵ I. E. Zadeh, A. W. Elshaari, K. D. Jns, A. Fognini, D. Dalacu, P. J. Poole, M. E. Reimer, and V. Zwiller, “Deterministic Integration of Single Photon Sources in Silicon Based Photonic Circuits,” *Nano Lett.* **16**, 2289–2294 (2016).
 - ¹⁶ S. L. Mouradian, T. Schrder, C. B. Poitras, L. Li, J. Goldstein, E. H. Chen, M. Walsh, J. Cardenas, M. L. Markham, D. J. Twitchen, M. Lipson, and D. Englund, “Scalable Integration of Long-Lived Quantum Memories into a Photonic Circuit,” *Phys. Rev. X* **5**, 031 009 (2015).
 - ¹⁷ E. Murray, D. J. P. Ellis, T. Meany, F. F. Floether, J. P. Lee, J. P. Griffiths, G. A. C. Jones, I. Farrer, D. A. Ritchie, A. J. Bennett, and A. J. Shields, “Quantum photonics hybrid integration platform,” *Applied Physics Letters* **107**, 171 108 (2015).
 - ¹⁸ E. Bermdez-Urea, C. Gonzalez-Ballester, M. Geiselmann, R. Marty, I. P. Radko, T. Holmgaard, Y. Alaverdyan, E. Moreno, F. J. Garcia-Vidal, S. I. Bozhevolnyi, and R. Quidant, “Coupling of individual quantum emitters to channel plasmons,” *Nature Communications* **6**, 7883 (2015).
 - ¹⁹ A. W. Fang, H. Park, Y.-h. Kuo, R. Jones, O. Cohen, D. Liang, O. Raday, M. N. Sysak, M. J. Paniccia, and J. E. Bowers, “Hybrid silicon evanescent devices,” *Materials Today* **10**, 28–35 (2007).
 - ²⁰ The identification of any commercial product or trade name is used to foster understanding. Such identification does not imply recommendation or endorsement or by the National Institute of Standards and Technology, nor does it imply that the materials or equipment identified are necessarily the best available for the purpose.
 - ²¹ F. Marsili, V. B. Verma, J. A. Stern, S. Harrington, A. E. Lita, T. Gerrits, I. Vayshenker, B. Baek, M. D. Shaw, R. P. Mirin, and S. W. Nam, “Detecting single infrared photons with 93% system efficiency,” *Nature Photonics* **7**, 210–214 (2013).
 - ²² A. C. Dada, T. S. Santana, R. N. E. Malein, A. Koutroumanis, Y. Ma, J. M. Zajac, J. Y. Lim, J. D. Song, and B. D. Gerardot, “Indistinguishable single photons with flexible electronic triggering,” *Optica* **3**, 493 (2016).
 - ²³ M. Köllner and J. Wolfrum, “How many photons are necessary for fluorescence-lifetime measurements?” *Chemical Physics Letters* **200**, 199–204 (1992).